ZSWIM8 destabilizes many murine microRNAs and is required for proper embryonic growth and development

Charlie Y. Shi,[1,2,3] Lara E. Elcavage,[1,2,3] Raghu R. Chivukula,[4] Joanna Stefano,[1,2,3] Benjamin Kleaveland,[5] and David P. Bartel[1,2,3]

[1]*Howard Hughes Medical Institute, Cambridge, Massachusetts 02142, USA;* [2]*Whitehead Institute for Biomedical Research, Cambridge, Massachusetts 02142, USA;* [3]*Department of Biology, Massachusetts Institute of Technology, Cambridge, Massachusetts 02139, USA;* [4]*Center for Genomic Medicine, Massachusetts General Hospital, Boston, Massachusetts 02114, USA;* [5]*Department of Pathology and Laboratory Medicine, Weill Cornell Medical College, New York, New York 10021, USA*

MicroRNAs (miRNAs) pair to sites in mRNAs to direct the degradation of these RNA transcripts. Conversely, certain RNA transcripts can direct the degradation of particular miRNAs. This target-directed miRNA degradation (TDMD) requires the ZSWIM8 E3 ubiquitin ligase. Here, we report the function of ZSWIM8 in the mouse embryo. *Zswim8*$^{-/-}$ embryos were smaller than their littermates and died near the time of birth. This highly penetrant perinatal lethality was apparently caused by a lung sacculation defect attributed to failed maturation of alveolar epithelial cells. Some mutant individuals also had heart ventricular septal defects. These developmental abnormalities were accompanied by aberrant accumulation of more than 50 miRNAs observed across 12 tissues, which often led to enhanced repression of their mRNA targets. These ZSWIM8-sensitive miRNAs were preferentially produced from genomic miRNA clusters, and in some cases, ZSWIM8 caused a switch in the dominant strand or isoform that accumulated from a miRNA hairpin—observations suggesting that TDMD provides a mechanism to uncouple coproduced miRNAs from each other. Overall, our findings indicate that the regulatory influence of ZSWIM8, and presumably TDMD, in mammalian biology is widespread and consequential, and posit the existence of many yet-unidentified transcripts that trigger miRNA degradation.

[Supplemental material is available for this article.]

MicroRNAs (miRNAs) are ~22-nucleotide (nt) RNAs that associate with Argonaute (AGO) proteins to guide the repression of mRNAs. Within the miRNA–AGO complex, the miRNA recognizes target RNAs through base-pairing interactions, primarily to the miRNA seed region (miRNA nucleotides 2–8), whereas the AGO protein recruits deadenylases that accelerate deadenylation of the targeted mRNA, which typically promotes mRNA decay (Jonas and Izaurralde 2015; Bartel 2018; Eisen et al. 2020). miRNA-directed regulation is both pervasive and biologically important, in that each of the 90 most broadly conserved miRNA families has, on average, more than 400 preferentially conserved targets (Friedman et al. 2009), and for most of these families, loss of function in mice results in abnormalities that severely impact fitness (Bartel 2018).

Despite the well-established regulatory logic governing canonical miRNA–target interactions, in certain cases, the direction of this logic is reversed. In these cases, when a target RNA engages both the seed of the miRNA and its 3′ region through extensive base-pairing, the miRNA becomes destabilized (Ameres et al. 2010; Cazalla et al. 2010; Libri et al. 2012; Marcinowski et al. 2012; Xie et al. 2012; Lee et al. 2013; de la Mata et al. 2015; Bitetti et al. 2018; Ghini et al. 2018; Kleaveland et al. 2018; Sheu-Gruttadauria et al. 2019). A biological role for this phenomenon of target-direct miRNA degradation (TDMD) was first observed during infection by a gamma-herpesvirus, which expresses a noncoding transcript, HSUR1, that directs degradation of host miR-27, a miRNA that might otherwise limit viral replication (Cazalla et al. 2010). TDMD has since been found to be exploited by other herpesviruses that express unrelated transcripts that trigger degradation of specific host miRNAs (Libri et al. 2012; Marcinowski et al. 2012; Lee et al. 2013). More recently, cellular transcripts that direct degradation of endogenous miRNAs have been discovered. In a founding example of this endogenous TDMD, a site within the mouse *Nrep* mRNA directs degradation of miR-29b, which shapes the behavior of the animal, as does a site in an orthologous long noncoding RNA (lncRNA) in zebrafish (Bitetti et al. 2018). In another example, a site within the Cyrano lncRNA directs degradation of miR-7, which reduces the level of miR-7 by >97% in some mouse tissues, including the cerebellum (Kleaveland et al. 2018). Two other examples of endogenous TDMD have been reported from studies using cultured mammalian cells (Ghini et al. 2018; Li et al. 2021), and another six have been identified in *Drosophila* cells or embryos (Kingston et al. 2022; Sheng et al. 2023). For instance, a site within the *Drosophila* lncRNA Marge directs degradation of members of the miR-310 family, which is required for proper development of the embryonic cuticle (Kingston et al. 2022).

TDMD requires a Cullin–RING E3 ubiquitin ligase complex containing the substrate adapter ZSWIM8 (Han et al. 2020; Shi et al. 2020). In the current model of TDMD, this E3 ligase recognizes a distinct conformation assumed by the AGO–miRNA complex

Corresponding author: dbartel@wi.mit.edu
Article published online before print. Article, supplemental material, and publication date are at https://www.genome.org/cgi/doi/10.1101/gr.278073.123. Freely available online through the *Genome Research* Open Access option.

33:1482–1496 Published by Cold Spring Harbor Laboratory Press; ISSN 1088-9051/23; www.genome.org

when extensively paired to a trigger site (Sheu-Gruttadauria et al. 2019), which results in the polyubiquitination and proteasomal destruction of AGO, exposing the miRNA to cellular nucleases (Han et al. 2020; Shi et al. 2020).

The loss of ZSWIM8 causes not only increased accumulation of known TDMD substrates but also increased accumulation of other miRNAs, implicating these additional ZSWIM8-sensitve miRNAs as potential TDMD substrates. Thus far, 34 ZSWIM8-sensitve miRNAs have been identified in mouse or human cells (Li et al. 2020; Shi et al. 2020), 21 have been identified in *Drosophila* S2 cells or embryos (Shi et al. 2020; Kingston et al. 2022), and 10 have been identified in *Caenorhabditis elegans* gravid adults (Shi et al. 2020). These findings suggest that the scope of endogenous TDMD is broad and that this pathway provides a conserved mechanism by which diverse animal species shape the levels of their miRNAs. Indeed, the influence of ZSWIM8 quantitatively explains the short half-lives of most short-lived miRNAs in both mouse embryonic fibroblasts (MEFs) and *Drosophila* S2 cells (Shi et al. 2020).

Dorado (Dora), the ZSWIM8 ortholog in flies, is essential for viability (Kingston et al. 2022), but EBAX-1, the ortholog in *C. elegans*, is not (Wang et al. 2013). Perhaps TDMD mediates divergent biological functions in different animals, presumably through variation in the cohort of miRNAs targeted for degradation. Another possibility is that other roles of ZSWIM8 contribute to these different phenotypic outcomes. Indeed, mechanisms unrelated to miRNAs are reported for the EBAX-1/ZSWIM8-mediated promotion of proper neural development in *C. elegans* and mouse (Wang et al. 2013, 2023) and Dora-mediated promotion of proper hair formation in *Drosophila melanogaster* (Molina-Pelayo et al. 2022). Here, we examine the effects of ZSWIM8 on mouse embryonic development and miRNA accumulation.

Results

ZSWIM8 is required for perinatal viability

To assess the biological functions of ZSWIM8 in mice, we generated *Zswim8* loss-of-function mutant alleles using Cas9 and a guide RNA known to abrogate TDMD in cell culture (Shi et al. 2020). Four independent mouse lines were recovered, each bearing a frameshifted allele predicted to produce truncated protein with disrupted function (Fig. 1A). As heterozygotes (*Zswim8*$^{+/-}$), these mutant mice were grossly normal and fertile. No phenotypic differences were observed between the four mutant lines, and hence, they were combined and treated as identical.

After intercrossing *Zswim8*$^{+/-}$ mice and genotyping at the age of weaning (around postnatal day [P] 21), the ratio of heterozygous to wild-type offspring matched the Mendelian expectation, but no *Zswim8*$^{-/-}$ offspring were observed (Fig. 1B). In contrast, on the day of birth (P0) or at embryonic day (E) 18.5, the expected Mendelian ratios of the three *Zswim8* genotypes were observed (Fig. 1B), indicating that *Zswim8*$^{-/-}$ animals were born but died before weaning. Indeed, examination of *Zswim8*$^{-/-}$ P0 neonates revealed that (1) many, but not all, were dead at the time of observation; (2) nearly all, whether alive or dead, appeared cyanotic (Fig. 1C); (3) those that were alive at the time of observation died within several hours, often following a period of agonal breathing (Supplemental Video S1); and (4) most appeared smaller than their littermates. In contrast, wild-type and *Zswim8*$^{+/-}$ neonates appeared normal.

To quantify the size difference observed for *Zswim8*$^{-/-}$ mice, we weighed embryos dissected at E18.5, a day before their expected birth, to prevent potentially confounding differences in feeding. Whereas wild-type and *Zswim8*$^{+/-}$ embryos did not significantly differ in weight, *Zswim8*$^{-/-}$embryos were ~22% lighter (Fig. 1D).

ZSWIM8 is required for proper embryonic development of heart and lung

The cyanotic and respiratory-distress phenotypes of *Zswim8*$^{-/-}$ neonates suggested that these animals failed to achieve proper oxygenation after birth. Although this phenotype could arise from defects in a number of different physiological processes, we first examined the developmental anatomy of the cardiovascular and pulmonary systems.

Serial transverse sections of hearts at E18.5 revealed ventricular septal defects (VSDs) in three of four *Zswim8*$^{-/-}$ embryos examined, but not in their *Zswim8*$^{+/-}$ littermates (Fig. 2A). VSDs are one of the most commonly recognized congenital heart defects and sometimes cause cyanosis in human patients (Mavroudis et al. 2013). Although the VSDs might have contributed to the cyanosis observed in *Zswim8*$^{-/-}$ newborns, they did not appear sufficiently severe to explain the highly penetrant lethality. To search for additional defects that might contribute, we examined lung sections from E18.5 embryos that had never breathed air. Relative to lungs of *Zswim8*$^{+/-}$ littermates, lungs of *Zswim8*$^{-/-}$ embryos had a significant reduction in total airspace (Supplemental Fig. S1).

During the saccular phase of lung development, which begins at approximately E18.5, the distal tips of the airway arbor undergo airspace expansion to form saccules that are precursors to alveoli, the future sites of gas exchange (Herriges and Morrisey 2014). These developing alveoli are populated by the two major alveolar epithelial cell lineages: the alveolar type I (AT1) cells, which are squamous and form most of the gas-exchange surface area, and alveolar type II (AT2) cells, which produce and secrete pulmonary surfactant (Morrisey and Hogan 2010).

To examine the effect of ZSWIM8 loss on sacculation, we stained developing lungs from wild-type, *Zswim8*$^{+/-}$, and *Zswim8*$^{-/-}$ embryos for Podoplanin and Pro-surfactant C, markers of AT1 and AT2 cells, respectively. As expected, wild-type lungs underwent alveolar epithelial cell differentiation by E17.5 and the onset of airspace expansion at the distal tips at E18.5 (Morrisey and Hogan 2010; Wang et al. 2016). Whereas lungs from *Zswim8*$^{+/-}$ embryos resembled those of the wild type throughout E16.5–E18.5, those from *Zswim8*$^{-/-}$ embryos visibly diverged at E18.5, failing to undergo airspace expansion despite possessing approximately normal proportions of AT1 and AT2 cells (Fig. 2B). Notably, this defect was localized to the alveolar compartment, as airways, which do not stain positive for Podoplanin, appeared grossly normal across all genotypes (Fig. 2B). The airspace defect in the *Zswim8*$^{-/-}$ lungs persisted to E19.5 (Fig. 2B), suggesting that proper saccular development was impeded through the time of birth.

ZSWIM8 is required for proper maturation of alveolar epithelial cells

To more closely examine the cellular basis for the airspace-expansion defect, we dissociated whole lungs from two *Zswim8*$^{+/-}$ and three *Zswim8*$^{-/-}$ E18.5 embryos and performed single-cell RNA sequencing (scRNA-seq). After filtering for quality, data from 19,732 cells were captured and analyzed by UMAP embedding (McInnes et al. 2018) and unsupervised clustering.

For clusters representing most of these lineages, the two genotypes were similarly distributed (Fig. 3A; Supplemental Table S2). An exception of particular interest was the cluster corresponding to the lung epithelial lineage—characterized by expression of

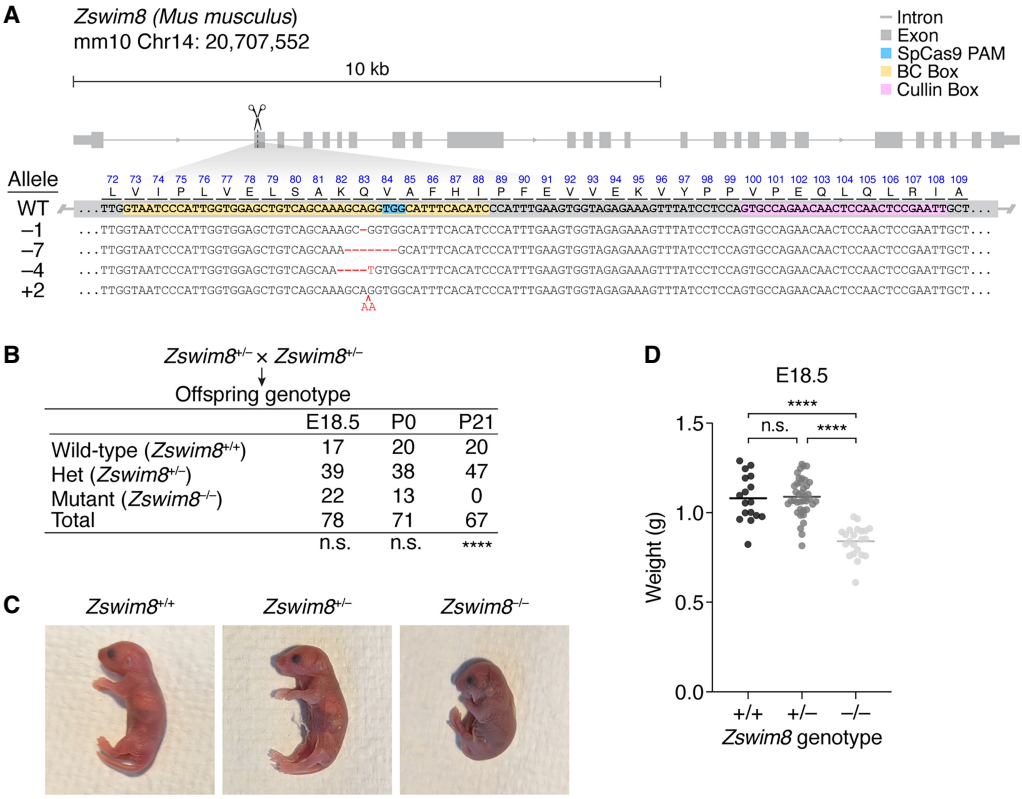

	E18.5	P0	P21
Wild-type (*Zswim8*$^{+/+}$)	17	20	20
Het (*Zswim8*$^{+/-}$)	39	38	47
Mutant (*Zswim8*$^{-/-}$)	22	13	0
Total	78	71	67
	n.s.	n.s.	****

Figure 1. Gross phenotypes of *Zswim8*$^{-/-}$ mice. (*A*) Organization of the murine *Zswim8* genomic locus. Shown *below* the gene model (thick gray boxes indicate the exonic coding sequence; thin gray boxes, exonic untranslated regions; gray lines, introns; blue box, Cas9 PAM; yellow box, annotated BC box motif; pink box, annotated Cullin box motif) are the genomic DNA sequences of the wild-type (WT) allele and four mutant alleles ("–1," "–7," "–4," and "+2"), as well as the amino acid sequence of the expected WT translation product. Blue text indicates the WT protein sequence; black text, WT DNA sequence; red text, insertions; and red dashes, deletions. (*B*) Penetrant lethality of *Zswim8*$^{-/-}$ animals. Shown are genotypes of offspring produced from intercrosses between *Zswim8*$^{+/-}$ parents. Offspring were counted at either embryonic day (E)18.5, postnatal day (P) 0, or P21. Differences from the Mendelian expectation were evaluated using the chi-square test (two-tailed): (n.s.) not significant, $P > 0.05$; (****) $P < 0.0001$. (*C*) Cyanotic phenotype of *Zswim8*$^{-/-}$ pups. Shown are P0 neonate siblings with the indicated genotypes, cropped from the same photograph. (*D*) Smaller size of *Zswim8*$^{-/-}$ embryos. Plotted are weights of E18.5 embryos produced from intercrosses between *Zswim8*$^{+/-}$ parents. Horizontal lines indicate the mean. Significance of differences were evaluated using ANOVA (Tukey's multiple comparisons test): (n.s.) not significant, $P > 0.05$; (****) $P < 0.0001$.

Nkx2-1 (Supplemental Fig. S2A; Herriges and Morrisey 2014), which gives rise to the major cell types of the alveoli. Within this cluster, *Zswim8*$^{-/-}$ cells were depleted from the periphery of the embedded space (Fig. 3B). Re-embedding and reclustering of this compartment revealed regions with a high expression of *Ager* and *Sftpb*, canonical markers for AT1 and AT2 cells, respectively (Fig. 3B), with peripheral subregions possessing near-exclusive expression of one or the other. These subregions likely represented populations of the more developmentally mature forms of these cell types, as evident from the enriched expression of other canonical marker genes within the corresponding clusters (clusters 3, 5, and 0) (Supplemental Fig. S2D). *Zswim8*$^{-/-}$ cells were depleted from these subregions, concentrating instead in intervening clusters (clusters 1, 7, and 8), in which they substantially outnumbered *Zswim8*$^{+/-}$ cells (Fig. 3B; Supplemental Fig. S2B). Of these, clusters 1 and 7 were the more populated and had intermediate expression of both canonical AT1 and AT2 lineage markers. Notably, cluster 1 appeared to bridge the AT1 and AT2 regions, and two of its top four most significant marker genes, *Ccn1* and *H19* (Supplemental Fig. S2D), were among the top five marker genes for an AT1 precursor state normally present at E17.5 (Fig. 3C; Frank et al. 2019). Cluster 7 was uniquely characterized by a high proportion of cells in the G_2/M phase (Supplemental Fig. S2C) and significantly enriched expression ($P < 10^{-5}$) of four out of five AT1 precursor markers, as well as for four out of five AT2 precursor markers (Fig. 3C; Frank et al. 2019). The expression patterns of these precursor markers generally corresponded well with our clustering (Supplemental Fig. S2E).

Together, these results supported a model in which the sacculation defect observed in *Zswim8*$^{-/-}$ lungs resulted from a failure of AT1 and AT2 precursors to properly differentiate into their respective mature forms after E17.5, causing a block in sacculation.

ZSWIM8 has a widespread impact on embryonic miRNA levels

To investigate the impact of ZSWIM8 on miRNA levels, we performed small RNA sequencing (sRNA-seq) on samples from the forebrain, hindbrain, eye, heart, lung, liver, stomach, kidney, intestine, skin, skeletal muscle, and placenta dissected from *Zswim8*$^{+/-}$ and *Zswim8*$^{-/-}$ E18.5 embryos. This stage was chosen to capture developmental differences in miRNA levels while avoiding secondary effects arising from the need of newborns to breath air.

The levels of miRNAs quantified for each tissue of the same genotype correlated well across two replicates (Supplemental Fig. S3A) and did not vary substantially in bulk abundance across *Zswim8* genotypes compared with internal spike-in controls (Supplemental Fig. S3F). To identify miRNAs that were significantly

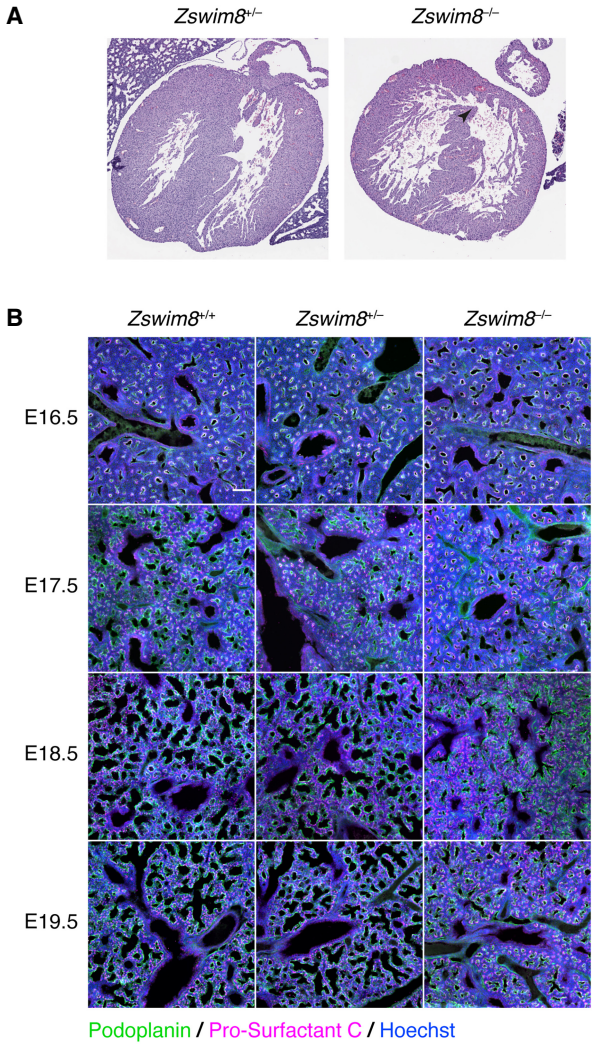

Figure 2. Tissue-level phenotypes of *Zswim8*$^{-/-}$ embryos. (*A*) Heart defect in *Zswim8*$^{-/-}$ embryos. Shown are representative images of H&E-stained transverse sections of hearts from *Zswim8*$^{+/-}$ and *Zswim8*$^{-/-}$ littermates at E18.5. Arrowhead points to a VSD. (*B*) Sacculation defect in *Zswim8*$^{-/-}$ embryos. Shown are lung sections from *Zswim8*$^{+/+}$, *Zswim8*$^{+/-}$, and *Zswim8*$^{-/-}$ embryos at the indicated developmental times immunostained for Podoplanin and Pro-surfactant C (green and magenta, respectively) and stained for DNA (Hoechst; blue). Scalebar represents 100 μm.

up-regulated in *Zswim8*$^{-/-}$ tissues, we used a statistical approach developed for detecting changes expected to be unidirectional, based on a bi-beta-uniform mixture (BBUM) model, which offers increased robustness to secondary effects, as well as false-discovery rate (FDR)–adjusted significance thresholds (Supplemental Fig. S3B; Wang and Bartel 2023).

The miRNAs that were significantly up-regulated by BBUM analysis (FDR-adjusted *P*-value < 0.05) were each further analyzed based on the behavior of its passenger strand, namely, the strand concurrently processed from the other arm of the miRNA precursor during miRNA biogenesis (Bartel 2018). Because TDMD occurs after the miRNA associates with AGO and dissociates from its passenger strand, authentic TDMD substrates increase upon loss of ZSWIM8 without a corresponding increase in their passenger strands (de la Mata et al. 2015). Accordingly, the ZSWIM8-sensitive miRNAs of each tissue were filtered to remove those that did not increase significantly more than their passenger strands upon *Zswim8* knockout. These miRNAs that were removed from the main set of ZSWIM8-sensitive miRNAs were designated as secondarily ZSWIM8-sensitive miRNAs. Although we cannot rule out the possibility that for some of these miRNAs both the miRNAs and their passenger strands were ZSWIM8-sensitive, we excluded them from the main set of ZSWIM8-sensitive miRNAs with the idea that their increased levels observed upon *Zswim8* knockout were most likely the result of increased pri-miRNA transcription or processing, or of some other secondary effect of ZSWIM8 loss that increased both the miRNAs and their passenger strands.

After applying these criteria to identify the ZSWIM8-sensitive miRNAs in each of the 12 tissues, we compared the results in different tissues to search for evidence of false positives and false negatives. When comparing across tissues, a few miRNAs appeared to have passed the annotation thresholds in a few individual tissues (typically one) owing to either transcriptional effects or extreme variability; these were removed from our set of ZSWIM8-sensitive miRNAs as suspected false positives (Supplemental Table S1). Another nine miRNAs did not meet our requirement for annotation as ZSWIM8-sensitive in any single tissue, yet were nonetheless broadly up-regulated (median $\log_2$ fold-change in *Zswim8*$^{-/-}$ >0.2), with increased levels exceeding those of their respective passenger strands broadly (in at least 11 out of 12 tissues) and substantially (median $\log_2$ magnitude >0.2); these nine broadly sensitive miRNAs were considered false negatives of our analyses of individual tissues and were added to the ZSWIM8-sensitive miRNAs of E18.5 embryos, bringing the total to 51 miRNAs from 43 miRNA families (Supplemental Table S1).

Among the 42 miRNAs classified as ZSWIM8-sensitive in one tissue, most also increased in other tissues, often enough to be independently classified as ZSWIM8-sensitive in the other tissues (Supplemental Fig. S3C). For those tissues in which their elevation was insufficient for independent classification but was nonetheless significantly greater than that observed for the passenger strand, we designated the miRNAs as marginally ZSWIM8-sensitive (Fig. 4A; Supplemental Fig. S3D; Supplemental Table S1). We anticipate that with more sensitive analyses (e.g., with more biological replicates), these miRNAs will ultimately be confidently classified as ZSWIM8-sensitive in these additional tissues.

ZSWIM8 can change the dominant miRNA strand or isoform

For nine miRNA duplexes (miR-335, miR-429, miR-466i, miR-497a, miR-544, miR-652, miR-764, miR-744, and miR-99b), the strand annotated as the passenger strand was ZSWIM8-sensitive (Supplemental Table S1). In these cases, we considered the ZSWIM8-sensitive strand as the miRNA and the other strand as the passenger strand for purposes of evaluating ZSWIM8 sensitivity. The miR-744 duplex was noteworthy in this respect, as its annotated passenger strand (miR-744-3p) was called as ZSWIM8-sensitive based on its broad albeit modest sensitivity in 11 of 12 tissues, whereas its annotated miRNA strand (miR-744-5p) is called as ZSWIM8-sensitive in induced mouse neurons (iNeurons) (Shi et al. 2020).

For five miRNA duplexes (miR-154, miR-335, miR-411, miR-450b, and miR-532), the strand that is normally less abundant became the more abundant strand upon loss of ZSWIM8 in a least one of the 12 tissues (Fig. 5A). For each of these miRNAs except miR-335, both strands were annotated as guides. Thus, tissue-selective ZSWIM8 sensitivity explained the previous report of miR-154 "arm switching" (Chiang et al. 2010), a phenomenon in which the

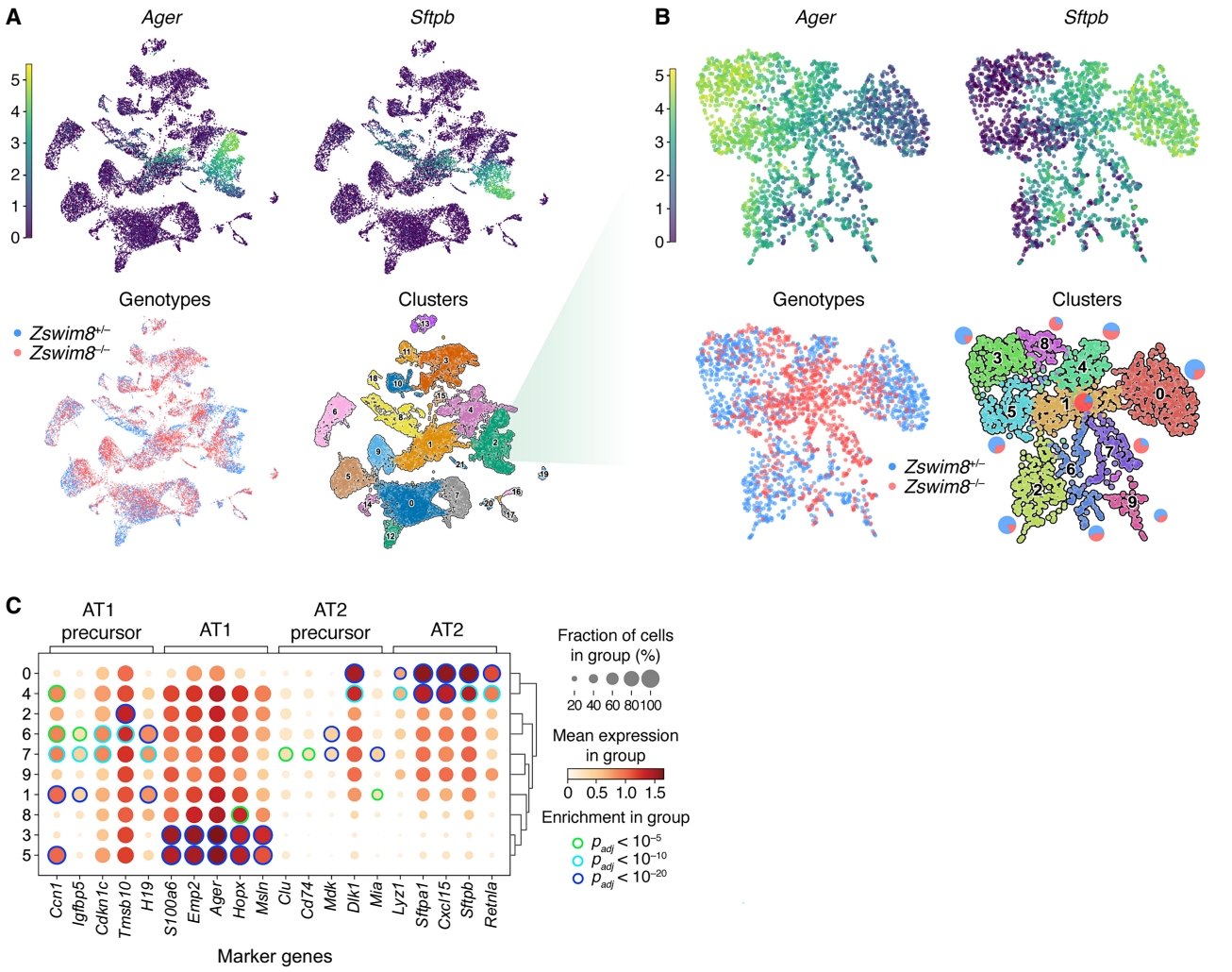

Figure 3. Improper maturation of epithelial cells from the lungs of *Zswim8*$^{-/-}$ embryos. (*A*) UMAP analysis of scRNA-seq data from all cells recovered from whole lungs of E18.5 embryos. Each point shown represents a cell from either *Zswim8*$^{+/-}$ ($n=2$) or *Zswim8*$^{-/-}$ ($n=3$) embryos. (*Top*) Coloring indicates expression of indicated genes; color bar is in units of ln(1 + CP10K). (CP10K) Counts per 10,000 unique counts. (*Bottom, left*) Coloring indicates genotype, with cells from embryos of the same genotype pooled together (blue indicates *Zswim8*$^{+/-}$; red, *Zswim8*$^{-/-}$). (*Bottom, right*) Coloring indicates cluster, with cluster numbers labeled and further characterized in Supplemental Figure S2A. (*B*) Re-embedded UMAP plots showing cells from cluster 2 of panel *A*. Pie charts adjacent to each cluster indicate percentages of cells of each genotype in that cluster. Otherwise, this panel is as in *A*. (*C*) Expression of marker genes (column labels) reported for AT1 precursor, AT1, AT2 precursor, and AT2 cells (Frank et al. 2019) in clusters identified in *B*. Row labels correspond to cluster numbers from *B*. The size of the discs indicates the fraction of cells in the cluster with detectable counts for the gene. The fill color of the discs indicates the mean expression in the cluster; color bar is in units of ln(1 + CP10K). Edge color of discs indicates statistical significance of enrichment for the gene in that cluster, relative to all clusters shown, as evaluated by the Wilcoxon rank-sum test, adjusted by the Benjamini–Hochberg method (green indicates $P_{adj} < 10^{-5}$; light blue, $P_{adj} < 10^{-10}$; dark blue, $P_{adj} < 10^{-20}$).

more abundant strand of a duplex differs in some contexts compared with others. Likewise, for miR-450b, the greater ZSWIM8 sensitivity of the 5p isoform in some tissues (e.g., eye) than in others (e.g., placenta) led to a newly identified example of arm switching (Fig. 5A).

In a related result, an isoform of miR-485-3p, which had an additional nucleotide at its 5′ end (a "+1" isoform, which we call miR-485.2-3p) and was previously unannotated by TargetScan7 (Agarwal et al. 2015), was even more ZSWIM8-sensitive than the annotated isoform (miR-485.1-3p) (Fig. 5B). As a result, upon ZSWIM8 loss, miR-485.2-3p accumulated to levels higher than those of either annotated guide strands (miR-485-5p and miR-485-3p) in each tissue examined (Fig. 5C).

An analysis of isoforms of all ZSWIM8-sensitive miRNAs, with the focus on isoforms that were either longer or shorter than the annotated isoform by 1 or 2 nt at the 5′ end (+1, +2, −1, and −2 isoforms), revealed that most ZSWIM8-senstive miRNAs had at least one such isoform of comparable ZSWIM8 sensitivity (Supplemental Fig. S4A), despite possessing an altered seed. Furthermore, as in the case of miR-485.1-3p, several other miRNAs (miR-20b-5p, miR-409-3p, miR-425-5p, and miR-551b-3p) had 5′ isoforms that were even more sensitive to ZSWIM8 loss than their respective annotated isoforms (Supplemental Fig. S4A), although none of these other miRNAs had isoforms that surpassed them in abundance in a *Zswim8*$^{-/-}$ tissue.

Taking the union of the 51 unique miRNAs identified as ZSWIM8-sensitive in our analyses of the 12 E18.5 tissues with the 29 miRNAs previously identified as ZSWIM8-sensitive in cultured MEFs and iNeurons (Shi et al. 2020) brought the total

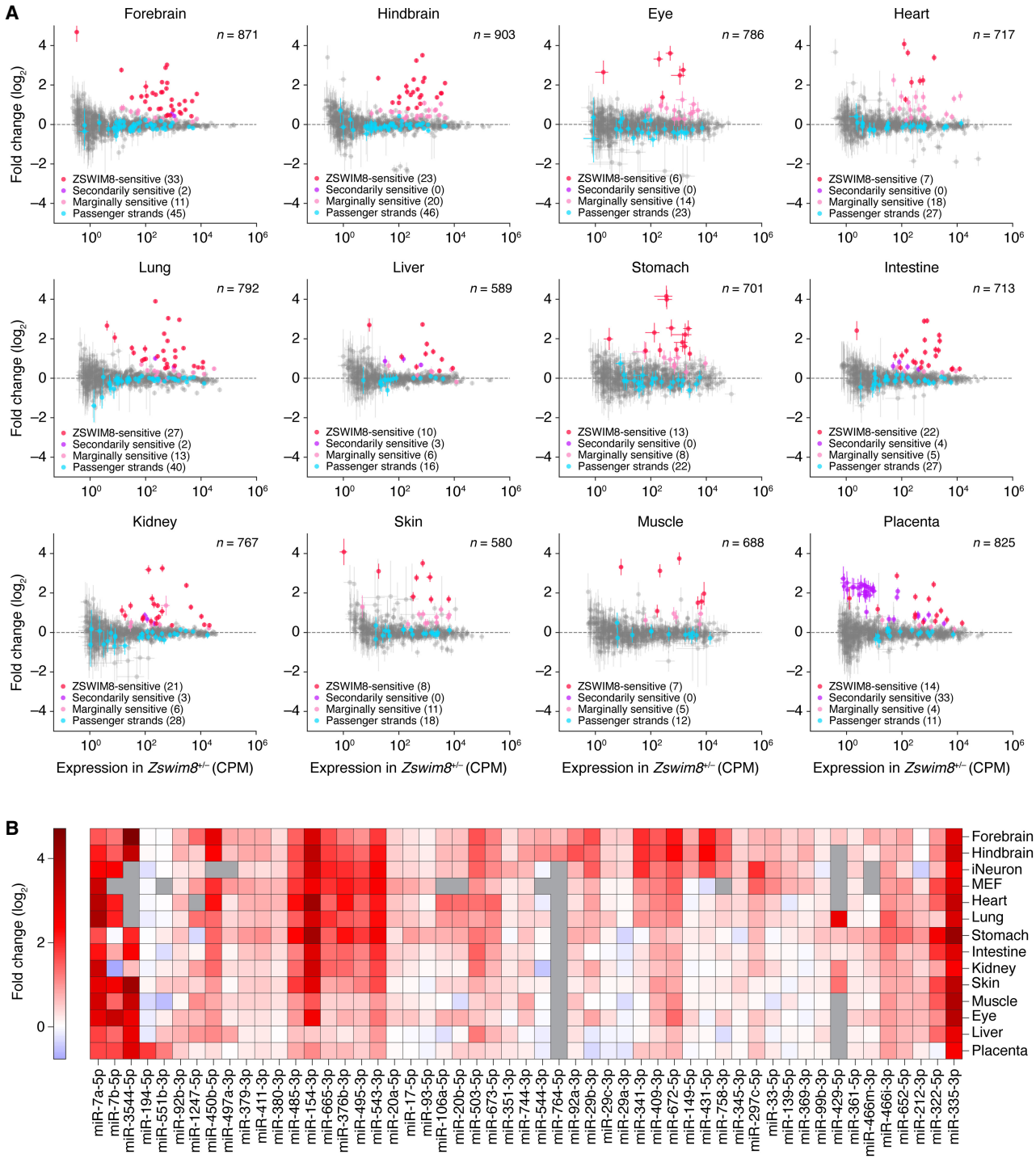

Figure 4. The impact of ZSWIM8 on miRNA levels in embryonic tissues. (*A*) The influence of ZSWIM8 on miRNA levels in the indicated tissues of mouse embryos, as determined by sRNA-seq. Plotted are fold-changes in miRNA (or passenger strand) levels observed when comparing the results for tissues from *Zswim8*$^{-/-}$ E18.5 embryos with those from *Zswim8*$^{+/-}$ E18.5 embryos (error bars, SE of two biological replicates). Red denotes ZSWIM8-sensitive miRNAs; purple, secondarily ZSWIM8-sensitive miRNAs (and their passenger strands); pink, marginally ZSWIM8-sensitive miRNAs; blue, passenger strands of sensitive and marginally sensitive miRNAs; and gray, all other annotated miRNAs or passenger strands that exceeded our expression threshold. (CPM) Counts per million, (*n*) total number of small RNAs analyzed. (*B*) The influence of ZSWIM8 on miRNAs classified as ZSWIM8-sensitive in at least one of the 12 embryonic tissues. The heatmap indicates fold-changes (key) observed when comparing the results for tissues from *Zswim8*$^{-/-}$ E18.5 embryos with those from *Zswim8*$^{+/-}$ E18.5 embryos (Supplemental Table S1). Also included are results for these same miRNAs observed after polyclonal *Zswim8* knockout in MEFs and iNeurons (Shi et al. 2020), as well as results for two miRNAs that were called as ZSWIM8-sensitive in at least one of those cell lines and were marginally ZSWIM8-sensitive in at least one embryonic tissue (miR-93-5p and miR-297c-5p). Gray squares indicate contexts in which the number of miRNA reads did not exceed the detection threshold of 5 CPM in each library prepared from the corresponding tissue. miRNAs were initially ordered by hierarchical clustering based on correlation, and then, a few manual adjustments were made to correct for clustering errors attributed to sparse data.

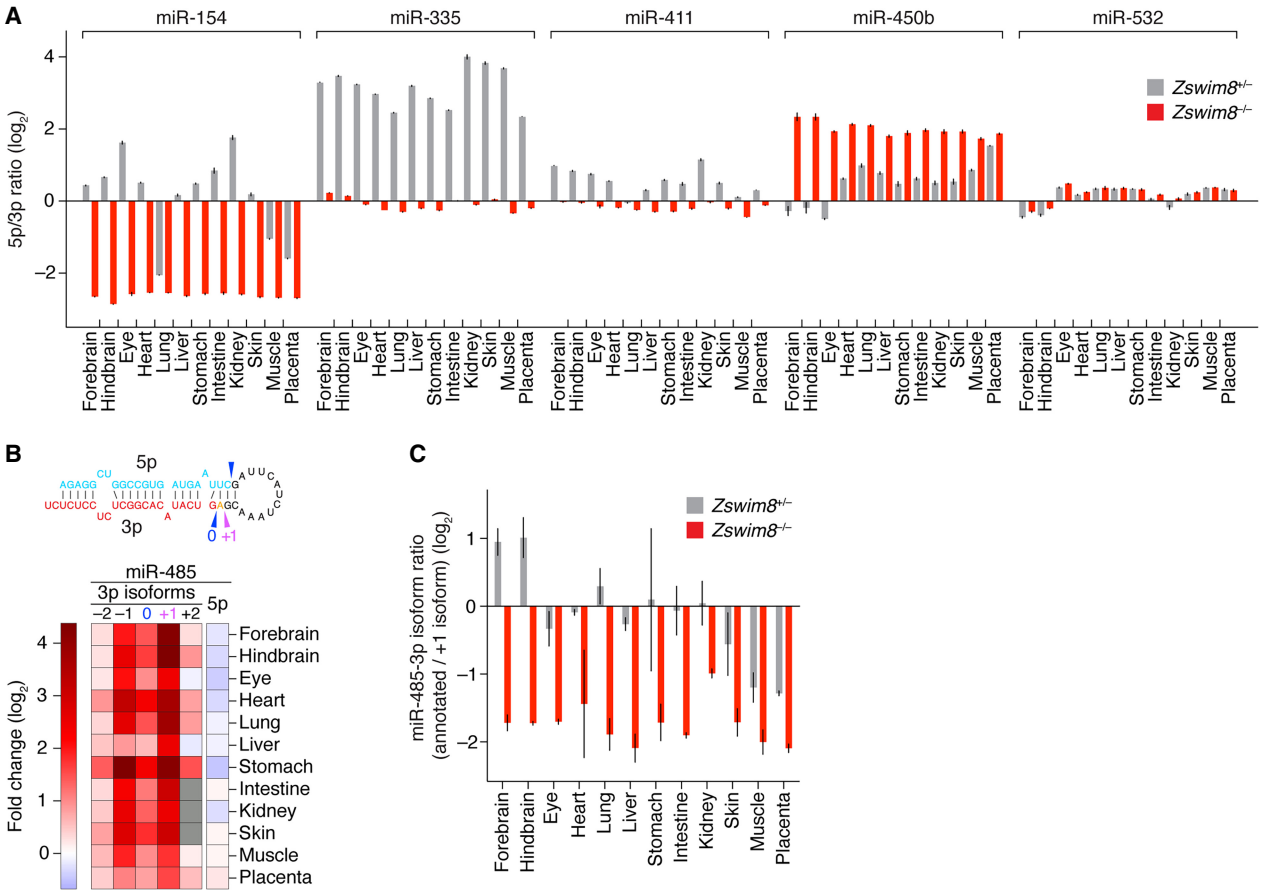

Figure 5. Influence of ZSWIM8 on miRNA isoform abundance and arm switching. (*A*) The influence of ZSWIM8 on the relative abundances of the two strands of miRNA duplexes. Plotted are ratios of the mean levels of 5p and 3p strands for the indicated miRNA duplexes in the indicated tissues, as quantified by sRNA-seq (error bars, error propagated from SE of two biological replicates). (*B*) The influence of ZSWIM8 on the abundances of miR-485-3p isoforms in the indicated tissues of mouse embryos, as determined by sRNA-seq. The heatmap indicates fold-changes (key) observed when comparing the results for tissues from *Zswim8*$^{-/-}$ E18.5 embryos with those from *Zswim8*$^{+/-}$ E18.5 embryos, as in Figure 4B. The −2, −1, 0, +1, and +2 labels indicate 5′ isoforms of miR-485-3p, with −1 and −2 denoting isoforms with 1- and 2-nt 5′ truncations, respectively; +1 denoting an isoform with 1-nt templated extension (miR-485-3p.2); and +2 denoting an isoform with 2-nt templated extension—all relative to the annotated isoform (miR-485-3.1p), denoted as 0. The inferred Dicer-processing sites that generated the annotated (0) and +1 miR-485-3p isoforms (as well as the annotated miR-485-5p strand) from the miR-485 precursor are indicated with arrowheads in the schematic *above* the heatmap. The annotated and +1 isoforms are emphasized because these were the two 3p isoforms with highest abundance across all tissues examined. (*C*) The influence of ZSWIM8 on the relative abundances of the annotated and +1 isoforms of miR-485-3p. Plotted are ratios of the two isoforms in *Zswim8*$^{+/-}$ and *Zswim8*$^{-/-}$ embryonic tissues, as quantified by sRNA-seq (error bars, error propagated from SE of two biological replicates).

number of ZSWIM8-sensitive miRNAs identified in mouse cells to 58, representing 48 miRNA families. A summary of the ZSWIM8-sensitivity profiles for the 53 miRNAs found to be at least marginally sensitive in embryonic tissues revealed distinct, context-specific patterns of sensitivity (Fig. 4B). For example, some miRNAs, such as miR-431-5p, were preferentially ZSWIM8-sensitive in brain or iNeuron samples despite being widely expressed, whereas others, such as miR-335-3p, were broadly and highly ZSWIM8-sensitive in every context examined. This pattern of sensitivity was unlikely to be explained by tissue-level differences in *Zswim8* mRNA expression, in that *Zswim8* mRNA levels were largely uniform across these tissues although somewhat higher in the brain and markedly lower, but still present, in the liver (Supplemental Fig. S6A). With the exception of placenta, *Zswim8* mRNA was slightly elevated in *Zswim8*$^{-/-}$ tissues, hinting at feedback mechanisms governing its expression (Supplemental Fig. S6A). In sum, when considering the marginally sensitive miRNAs together with the sensitive miRNAs, each tissue analyzed had at least 12 miRNAs that had ZSWIM8 sensitivity resembling that of TDMD substrates, with the numbers for brain and lung tissues exceeding 40. These results implied that TDMD has a widespread influence in shaping miRNA levels throughout the embryo.

ZSWIM8-sensitive miRNAs are disproportionately produced from genomic clusters

Many miRNAs are produced from genomic clusters, wherein multiple hairpin-encoding miRNA genes are juxtaposed and often transcribed together in polycistrons. Such an arrangement enables coexpression (Baskerville and Bartel 2005) and can facilitate the processing of suboptimal miRNA hairpins (Fang and Bartel 2020; Hutter et al. 2020; Shang et al. 2020). However, situations might arise in which decoupling the expression of cluster members could be advantageous, and TDMD might, in some cases, help enact this decoupling. To explore this possibility, we examined the genomic distribution of the 58 mouse miRNAs called as ZSWIM8-sensitive

in embryos or cell lines, which corresponded to 61 miRNA hairpin loci. Of these 61 loci, 44 (or 72%) mapped to miRNA clusters (Fig. 6A–C), defined as regions in which adjacent miRNA genes were separated by no more than 10 kb. Because ~46% of miRNAs derived from clusters, the fraction of ZSWIM8-sensitive miRNAs that derived from clusters was significantly higher than expected by chance (Fig. 6D).

Seventeen ZSWIM8-sensitive miRNAs derived from the mammal-specific, imprinted *Dlk1–Dio3* locus on Chromosome 12, which encodes about 116 mature miRNA strands produced from about 58 hairpins, most of which are expressed from the maternal allele (Fig. 6A; da Rocha et al. 2008). Of these 17, 12 derived from the maternally expressed *Mirg* gene, which encodes 76 mature miRNA strands produced from 38 hairpins thought to be transcribed as a single polycistronic transcript. The remaining five derived from an upstream region of the *Dlk1–Dio3* locus, in the vicinity of the maternally expressed *Meg3* gene, although one of these, miR-3544-5p, which had the greatest sensitivity of all ZSWIM8-sensitive miRNAs (Fig. 4B; Supplemental Table S1), derived from the opposite strand, several kilobases downstream from *Rtl1*, an imprinted gene predominantly expressed from the paternal allele (Seitz et al. 2003). Because many miRNAs of the *Dlk1–Dio3* locus are related to each other, multiple ZSWIM8-sensitive members might share a common trigger RNA. Supporting this idea, some pairs of miRNAs from this locus had similar patterns of sensitivity to ZSWIM8 across different tissue/cellular contexts (e.g., miR-495-3p and miR-543-3p; miR-379-3p and miR-411-3p) (Fig. 4B). In another example of an imprinted miRNA cluster encoding ZSWIM8-sensitive miRNAs, the rodent-specific, paternally expressed miRNA cluster within the *Sfmbt2* gene (Supplemental Fig. S5; Inoue et al. 2017) contained two ZSWIM8-sensitive miRNAs (miR-466m-3p and miR-297c-5p).

Other ZSWIM8-sensitive miRNAs derived from three paralogous clusters: the miR-17~92 cluster, the miR-106a~363 cluster, and the miR-106b~25 cluster (Fig. 6B). Across these three clusters, most members of the miR-17 family (miR-17, miR-20a, miR-106a, miR-20b, and miR-93) were ZSWIM8-sensitive, the exception being miR-106b. Also sensitive was miR-92a, which is produced from both the miR-17~92 and miR-106a~363 clusters, although among the other four members of the miR-92 family (miR-92b, miR-25, miR-363, and miR-367), only miR-92b was also ZSWIM8-sensitive (Fig. 6B).

Other ZSWIM8-sensitive miRNAs included three miRNAs from the miR-322~450b cluster (miR-322-5p, miR-503-5p, and miR-450b-5p). These were ZSWIM8-sensitive in nearly every context examined (Fig. 6C). Nonetheless, they each had different patterns of sensitivity, suggesting that different triggers acted upon them, even though miR-322-5p and miR-503-5p have similar seed sequences.

ZSWIM8 reduces repression of targets of ZSWIM8-sensitive miRNAs

We next examined the consequences of these widespread changes in miRNA levels on the transcriptomes of tissues collected from *Zswim8*$^{-/-}$ embryos. For about half of the tissues, the effects were modest overall, with only a small number of individual mRNAs passing our significance threshold for differential expression (Supplemental Fig. S6D). In the heart, lung, liver, skin, and placenta, the number of differentially expressed mRNAs was greater, ranging in the tens to hundreds. The most widespread changes occurred in the lung, presumably, in part, a consequence of perturbed lung epithelial development (Fig. 3B). In most tissues, more mRNAs significantly decreased than increased (Supplemental Fig. S6D), suggesting that aberrant persistence of ZSWIM8-sensitive miRNAs could be causing some of these changes.

To assess this possibility, we examined predicted targets of the families of ZSWIM8-sensitive miRNAs whose members collectively increased the most upon ZSWIM8 loss (Supplemental Fig. S6E). Across the tissues, the most affected families varied in identity, with the most affected family increasing the total miRNA pool by 0.5%–2% (Supplemental Fig. S6E). For miR-7, the family most affected in forebrain, the levels of mRNAs predicted to be most susceptible to miR-7-mediated repression (i.e., the top predicted targets) tended to decrease, albeit modestly, in the forebrain upon loss of ZSWIM8, as expected if elevated levels of miR-7 caused increased repression of its regulatory targets ($P < 0.001$, Wilcoxon's rank-sum test) (Fig. 7A). Evidence for enhanced repression was also detected among the larger set of mRNAs with conserved sites to miR-7 (conserved predicted targets, $P < 0.05$) and among the even larger set with any 7- to 8-nt canonical site to miR-7 (all predicted targets, $P < 0.001$), albeit with even smaller median fold-changes than that observed for the top predicted targets (Fig. 7A). These results resembled those observed upon mutation of Cyrano, which directs ZSWIM8-dependent degradation of miR-7 (Kleaveland et al. 2018; Han et al. 2020; Shi et al. 2020). Similar results were observed for the predicted targets of the most affected miRNA family in the lung (miR-15) and heart (miR-503) (Fig. 7A). Indeed, for 10 of the 12 tissues examined, analogous evidence for enhanced repression by the most affected miRNA was observed, and this evidence often extended to the predicted targets of the second and third most affected miRNA families (Fig. 7B). These results indicated that loss of ZSWIM8 causes modest, but widespread dysregulation of gene expression across many different tissues, and suggested that these changes are driven by overaccumulation of miRNAs presumed to be endogenous substrates of TDMD.

As expected, one of the transcripts reduced most upon ZSWIM8 loss was the brain-enriched circular RNA *Cdr1as* (Supplemental Fig. S6B). This circular RNA has 130 sites to miR-7 (Hansen et al. 2013; Memczak et al. 2013) and is the transcript most affected by mutation of Cyrano (Kleaveland et al. 2018). Cyrano was also sensitive to loss of ZSWIM8, decreasing in all 12 tissues examined from *Zswim8*$^{-/-}$ embryos (Supplemental Fig. S6C), despite the fact that mutations that either reduce miR-7 or disrupt the site that normally directs ZSWIM8-dependent miR-7 degradation do not impact Cyrano levels in any tissues examined (Kleaveland et al. 2018). Perhaps repression of Cyrano mediated by the intact site is kinetically disfavored compared with TDMD, but without ZSWIM8, this repression has time to occur, as proposed for analogous cases in *Drosophila* (Kingston et al. 2022). Alternatively, accumulation of other miRNAs in the absence of ZSWIM8 might cause increased destruction of Cyrano. Indeed, Cyrano harbors an apparently functional regulatory site to the miR-92 family (Li et al. 2020), which includes ZSWIM8-sensitive miRNAs that were broadly elevated across *Zswim8*$^{-/-}$ tissues, especially the brain (Fig. 4B; Supplemental Fig. S6E).

Discussion

Phenotypic consequences of *Zswim8* knockout

The severity and penetrance of the *Zswim8* loss-of-function phenotype resembles that observed in *Drosophila*, in which point mutants in the *Zswim8* ortholog *Dora* are lethal (90%–100%

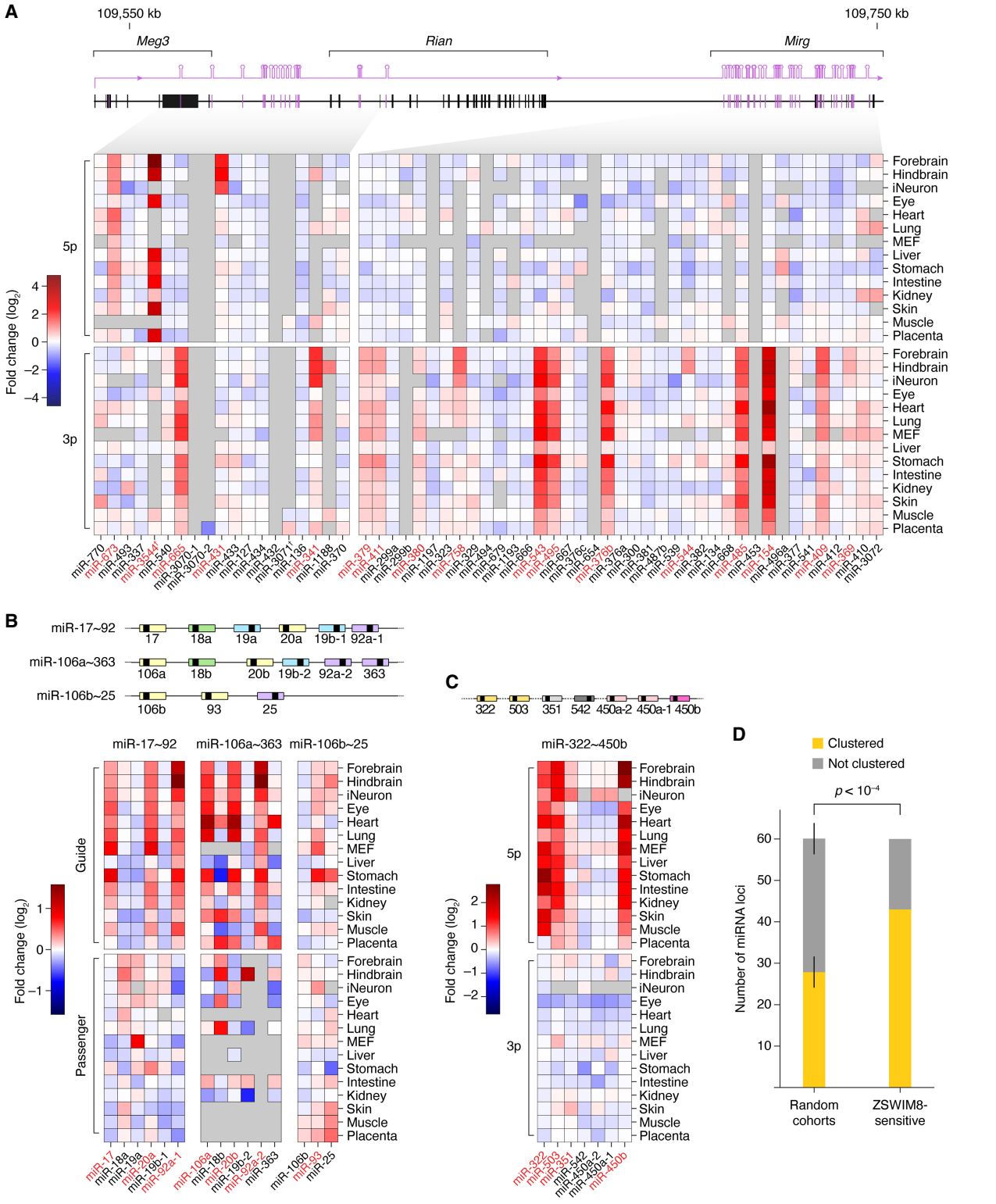

Figure 6. Genomic organization of ZSWIM8-sensitive miRNAs. (*A*) Clustered miRNA genes of the imprinted *Dlk1–Dio3* locus, which produces a preponderance of ZSWIM8-sensitive miRNAs. Shown are fold-changes in miRNA levels observed in *Zswim8*$^{-/-}$ tissues, relative to *Zswim8*$^{+/-}$ tissues from E18.5 embryos, as well as in MEFs and iNeurons (Shi et al. 2020). The miRNAs are ordered by position within the cluster and organized by strand. Each plotted value is the average of two biological replicates. Red text denotes ZSWIM8-sensitive miRNAs; dagger, miRNA apparently derived from the antisense strand of the paternal allele. (*B*) The miR-17~92 cluster and two paralogous clusters. Otherwise, as in panel *A*. (*C*) The miR-322~450b cluster. Otherwise, as in panel *A*. (*D*) A tendency of ZSWIM8-sensitive miRNAs to derive from clustered miRNA genes. The bar plots show the proportion of miRNA loci produced from a miRNA cluster for the set of 61 loci encoding ZSWIM8-sensitive miRNAs compared with random cohorts of the same size drawn without replacement from the set of all miRNA loci. Error bars, SD across 10,000 random cohorts. The *P*-value was calculated by hypergeometric test.

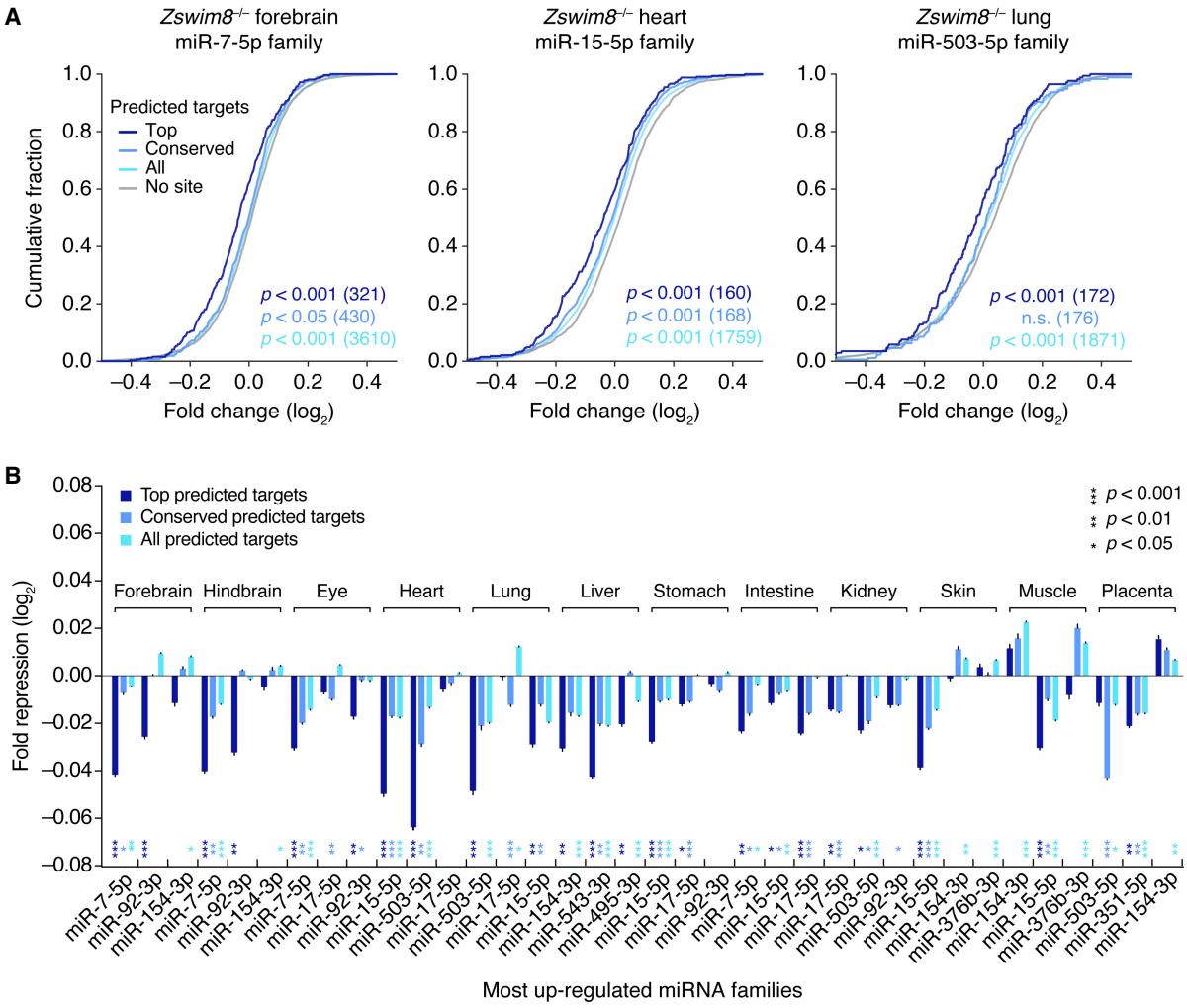

Figure 7. Increased repression of predicted targets of ZSWIM8-sensitive miRNAs upon loss of ZSWIM8. (*A*) Increased repression of predicted targets of the miRNA family whose members increase the most in embryonic forebrain (*left*), heart (*middle*), and lung (*right*). Plotted are cumulative distributions of mRNA fold-changes in indicated tissues of *Zswim8*$^{-/-}$ E18.5 embryos, relative to *Zswim8*$^{+/-}$ embryos, for each of four sets of mRNAs: top predicted targets (top; dark blue), conserved predicted targets (conserved; medium blue), and all predicted targets (all; light blue) of the indicated miRNA family, as well as transcripts containing no canonical site to that family, which were 3′-UTR length-matched to transcripts in the set of all predicted targets and randomly sampled at a five-to-one ratio (no site; gray). *P*-values were calculated (Wilcoxon's rank-sum test) comparing results for each set of predicted targets and its length-matched no-site cohort; for clarity, only the no-site cohort for the set of all predicted targets is shown. (*B*) Increased repression of predicted targets of the three miRNA families whose members collectively increased the most in the indicated tissues from *Zswim8*$^{-/-}$ embryos, relative to that of *Zswim8*$^{+/-}$ embryos, excluding miR-335-3p, which was a passenger strand that did not possess confidently predicted conserved targets (Friedman et al. 2009). To summarize the degree of miRNA-mediated repression, the median fold-change of the set of predicted targets was normalized to that of its length-matched no-site cohorts (error bars, SE of the mean from 21 independent no-site cohorts). For each such sampling, a *P*-value was calculated as in *A*, and the median *P*-value from all samples is shown for each family and each tissue, with coloring corresponding to the target set.

penetrance, depending on the allele and genetic background), with most individuals dying during embryonic or early larval development (Kingston et al. 2022). In contrast, null mutants of the *C. elegans* ortholog, *ebax-1*, are viable, albeit with defects in axon guidance, locomotion, egg laying, and male mating (Wang et al. 2013), suggesting that ZSWIM8 plays varied biological roles across metazoa. The extent to which phenotypes observed in these different animals arise from the loss of TDMD, rather than some other function of ZSWIM8, is still an open question. Indeed, ZSWIM8 is proposed to regulate neural development, myogenesis, and actin dynamics through mechanisms that do not involve TDMD (Wang et al. 2013, 2023; Okumura et al. 2021; Molina-Pelayo et al. 2022).

In mice, the lung sacculation defect observed in *Zswim8*$^{-/-}$ embryos presumably caused the perinatal lethality, with perhaps some contribution from the heart VSD. We note that at E18.5, the lungs of *Zswim8*$^{-/-}$ embryos resembled those of *Hdac3* mutants, in which AT1 cells appear to have an autonomous spreading defect caused by elevated expression of the miR-17∼92 cluster in lung epithelial cells, resulting in failure to properly sacculate and partially penetrant perinatal lethality (Wang et al. 2016). *Hdac3* mutants also have increased expression of members of the *Mirg* locus, although the consequences of this increase have not been determined (Wang et al. 2016). Moreover, expression of the miR-17∼92 cluster decreases over the course of embryonic development, and transgenic overexpression of this cluster in lungs as

they begin to develop causes a similar sacculation defect (Lu et al. 2007). These findings, combined with our observation that the levels of some members of the miR-17~92 cluster (and its paralogous clusters), as well of the *Mirg* cluster, significantly increase in *Zswim8*$^{-/-}$ lungs, suggested that the sacculation defect observed upon ZSWIM8 loss might be caused by the increased levels of these ZSWIM8-sensitive miRNAs.

One method of testing this hypothesis is to examine whether genetically offsetting the accumulation of these families can rescue the *Zswim8*$^{-/-}$ phenotype. This type of rescue implicates the targeted degradation of the miR-3 family in contributing to the lethality observed upon losing TDMD in flies (Kingston et al. 2022), and it implicates increased expression of the miR-17~92 cluster in contributing to the sacculation phenotype of *Hdac3* mutants (Wang et al. 2016). However, we have not observed clear rescue of the *Zswim8*$^{-/-}$ perinatal lethality, lung sacculation, or embryonic growth phenotypes (scoring for either cyanosis and survival rates at birth or lung histology and embryonic weights at E18.5) in animals with deletions designed to reduce the levels of key ZSWIM8-sensitive miRNAs, including miR-17~92$^{\Delta 17,18,92/+}$, miR-106b~25$^{-/-}$, maternal *Mirg*$^{-}$, and miR-322~351$^{-/-}$ (Ventura et al. 2008; Llobet-Navas et al. 2014; Han et al. 2015; Marty et al. 2016). Although we cannot rule out the possibility that the sacculation defect stemmed from loss of a non-TDMD ZSWIM8 function, we suspect that this failure to rescue was instead because we did not reduce the relevant combination of miRNAs to the levels required to offset the effects of ZSWIM8 loss. The molecular basis of the sacculation defect can be revisited once the trigger sites that direct miRNA degradation are identified and mutated, as has been performed in a few cases in the mouse, zebrafish, and *Drosophila* (Bitetti et al. 2018; Kleaveland et al. 2018; Kingston et al. 2022). Such experiments would elevate ZSWIM8-sensitive miRNAs to the status of validated TDMD substrates and open new opportunities for exploring the biological roles of this pathway.

Sensitivities of miRNAs to ZSWIM8

We found 51 miRNAs, representing 43 miRNA families, to be ZSWIM8-sensitive in at least one of the 12 embryonic tissues examined. These 51 included 22 that had previously been identified in MEFs or iNeurons (Shi et al. 2020) but not seven others that were only identified in the cell lines. They also did not include miR-30b/c or miR-221/222, which had previously been reported to be TDMD substrates in 3T9 mouse fibroblasts and three human cell lines, respectively (Ghini et al. 2018; Li et al. 2021). Perhaps more sensitive approaches focusing on purer cell populations, or examination of other life stages, will unearth evidence that these miRNAs are TDMD substrates in the animal.

Despite our use of miRNA fold-change when reporting ZSWIM8 sensitivity, this metric does not tell the whole story. Increasing production of a miRNA undergoing TDMD can lower the fold-change of the miRNA but increase the number of miRNA molecules that are degraded (de la Mata et al. 2015). Thus, miRNAs that undergo the greatest fold-changes upon loss of TDMD might not be the ones with the most vigorous or the most biologically consequential turnover. Indeed, when analyzing the effects of ZSWIM8 loss on predicted miRNA targets, we found that the absolute change in miRNA level was more consequential than the fold-change.

Our analysis of 5′ isoforms indicated that most ZSWIM8-sensitive miRNAs had at least one isoform of comparable or, in some cases, even greater sensitivity (Supplemental Fig. S4A). In aggregate, these ZSWIM8-sensitive isoforms included both 5′ truncations (−1 and −2 isoforms) and 5′ extensions (+1 and +2 isoforms), and for some individual ZSWIM8-sensitive miRNAs (e.g., miR-7a-5p, miR-503-5p, and miR-92a-3p), isoforms of both varieties were sensitive. The most intriguing example of 5′ isoform sensitivity was miR-485.2-3p, which is annotated as a minor isoform yet produced at a level sufficient to become the major isoform upon loss of ZSWIM8.

The ZSWIM8-sensitive major and minor 5′ isoforms often had similar patterns of sensitivity across tissues (Supplemental Fig. S4A), as expected if their degradation was directed by the same trigger. The idea that the shifted pairing of 5′ isoforms is compatible with TDMD, even though it often disrupts perfect seed pairing (as illustrated for Cyrano and miR-7 isoforms) (Supplemental Fig. S4B), suggests that TDMD might be more tolerant of imperfect seed pairing than currently appreciated. Perhaps the extensive 3′ pairing required to achieve the conformation suitable for TDMD provides binding affinity sufficient to compensate for seed mismatches.

Many questions abound concerning the endogenous regulatory functions of ZSWIM8-mediated control of miRNA stabilities through TDMD. Our work provided evidence for possible roles for this pathway in decoupling the ultimate expression of certain miRNAs from that of other RNAs with which they share common production. An extreme example of this can be found in *Mirg*, which contains the largest miRNA cluster in the mammalian genome and is part of the imprinted, maternally expressed *Dlk1–Dio3* region on Chromosome 12 (Fig. 6A). *Mirg* miRNAs are thought to antagonize the paternal expression program (Whipple et al. 2020), and *Mirg* knockout phenotypes (observed when the mutant allele is maternally inherited) include partially penetrant neonatal lethality, owing in part to metabolic defects, as well as anxiety-related behavior in adulthood (Labialle et al. 2014; Marty et al. 2016). We identified 12 ZSWIM8-sensitive miRNAs produced from *Mirg* and identified another five miRNAs from elsewhere in the greater imprinted region—all but one of which was maternally expressed (Fig. 6A). The directed degradation of these clustered miRNAs, while serving a decoupling function, might also have evolved as a means to favor paternal interests in the parental genomic conflict that drives mammalian genomic imprinting. We also observed imprinting in the opposite direction for the ZSWIM8-sensitive miRNAs of the *Sfmbt2* cluster (Supplemental Fig. S5) and for miR-335-3p, which are paternally expressed (Hiramuki et al. 2015; Inoue et al. 2017). The identification of triggers for these miRNAs would aid in evaluating the conflict model; for example, preferential expression of triggers from the other parent would provide further evidence of the deployment of TDMD in parental conflict.

Another example of decoupling mediated by ZSWIM8 was that of separating the expression of the two strands produced together from the same miRNA hairpin. Although preferences in AGO association play an important role in setting the balance of the two strands (Khvorova et al. 2003; Schwarz et al. 2003), our results showed that ZSWIM8 can push this balance in either direction: in most cases, restraining accumulation of strands apparently favored to associate with AGO, but in some cases (nine of 58 murine ZSWIM8-sensitive miRNAs) further reducing strands annotated as passengers (Supplemental Table S1). This latter mode might reduce unwanted activity of passenger strands in situations in which the asymmetry of AGO association is suboptimal. In other instances, both strands arising from a duplex are annotated as guides, each with a distinct cohort of targets; here, analogous to the case of clustered miRNAs, the obligate coproduction of two functional miRNAs might present another need for

strand-specific regulation in order to accommodate varied cellular contexts within an organism, some of which might be advantaged by the presence of both strands; others, not. Accordingly, we identified 14 ZSWIM8-sensitive miRNAs of this variety (Supplemental Table S1), including five cases in which ZSWIM8 activity caused arm switching (Fig. 5A).

Because our study focused on late embryonic development, it did not address the question of whether mammals undergo early ZSWIM8-dependent clearance of early-embryonic miRNAs, as occurs in *Drosophila* and *C. elegans* (Shi et al. 2020; Donnelly et al. 2022; Kingston et al. 2022). Future studies on the impact of ZSWIM8 during windows of developmental time could illuminate this, and temporal resolution might provide information on the biological processes affected by the degradation of particular miRNAs, including those identified in this study. Ultimately, a detailed appraisal of the biological processes regulated by endogenous TDMD will depend on genetic experiments perturbing the RNAs presumed to direct the degradation of ZSWIM8-sensitive miRNAs—most of which remain to be discovered. Identification of these putative endogenous trigger RNAs might also improve understanding of the sequence features—both of the binding sites themselves and also of more distal elements—that modulate TDMD efficacy and enable improved prediction and design of potent triggers. Our work expanding the known set of ZSWIM8-sensitive miRNAs and the anatomical scope of ZSWIM8 activity provides a foundation for these future efforts.

Methods

Mouse husbandry

Mice were group-housed in a 12-h/12-h light/dark cycle (light between 07:00 and 19:00) in a temperature-controlled room (21.1°C ± 1.1°C) at the Whitehead Institute for Biomedical Research with free access to water and food and were maintained according to protocols approved by the Massachusetts Institute of Technology committee on animal care. Euthanasia of adults was performed by CO_2 inhalation. Sex was not determined for embryos or neonatal pups, except where indicated. Embryos were weighed after being patted dry with a paper towel.

Generation of mutant mice

Mice with mutations in *Zswim8* were generated by injecting one-cell C57BL/6J embryos with Cas9 protein complexed with a sgRNA designed to cut within exon 2 of *Zswim8* (Fig. 1A). F_0 mice containing resulting deletions (1, 4, and 7 nt, respectively) and insertions (2 nt) were bred to C57BL/6J mice, and then, F_1 mice were crossed to generate lines with the desired heterozygous mutations (*Zswim8*$^{+/-}$). *Zswim8*$^{+/-}$ lines were maintained by breeding to C57BL/6J, and resulting heterozygous offspring were intercrossed to generate *Zswim8*$^{+/+}$, *Zswim8*$^{+/-}$, and *Zswim8*$^{-/-}$ embryos and neonates used in this study. No substantial phenotypic differences were observed between mice bearing each of four *Zswim8* alleles, which were used interchangeably in this study.

Genotyping

Genomic DNA was extracted from mouse ear punches using the HotSHOT method (Truett et al. 2000). For *Zswim8* mutants, PCR was performed with KAPA HiFi HotStart ReadyMix (Roche), and amplicons were purified (QIAquick PCR purification kit, Qiagen) and submitted for Sanger sequencing. Primers and expected amplicon sizes are listed in Supplemental Table S3.

RNA extraction

Tissues from E18.5 embryos were rapidly dissected after euthanasia of pregnant dams (CO_2) and flash-frozen using liquid nitrogen. Total RNA was extracted with TRI reagent according to the manufacturer's protocol with the following modifications. One to 2 mL of TRI reagent was added depending on the tissue volume, and the tissue was homogenized with a TissueRuptor (Qiagen). Phase separation was performed by adding 100 µL 1-bromo-3-chloropropane (Sigma-Aldrich) to 1 mL of homogenate. Precipitated RNA pellets were washed twice with 75% ethanol and resuspended in RNase-free water.

Bulk RNA-seq

Bulk RNA-seq data were generated from total RNA isolated from tissues dissected from one E18.5 *Zswim8*$^{+/-}$ embryo and one *Zswim8*$^{-/-}$ embryo from the same litter. This procedure was repeated with another litter, for $n = 2$ biological replicates. RNA-seq libraries were prepared from 1-µg samples of total RNA using the KAPA RNA HyperPrep kit with the RiboErase (HMR) kit (KAPA Biosystems) and sequenced on the Illumina NovaSeq platform with 50-nt paired-end reads. Reads were aligned to the mouse genome (mm10) using STAR v2.7.1a (Dobin et al. 2013) with the parameters "–runThreadN 24 –outFilterMultimapNmax 1 –outFilterMismatchNoverLmax 0.04 –outFilterIntronMotifs RemoveNoncanonicalUnannotated –outSJfilterReads Unique –outReadsUnmapped Fastx –quantMode GeneCounts –outSAMtype BAM SortedByCoordinate." Aligned reads were assigned to genes using annotations from RefSeq (downloaded August 3, 2022) and counted using htseq-count v0.6.1 (Anders et al. 2015). Further analyses were performed on genes passing the expression threshold of at least five counts in each of the four libraries from a tissue. Differential expression and significance levels were determined using DESeq2 v1.26.0 (Love et al. 2014) without the lfcShrink() function.

sRNA-seq

sRNA-seq data were generated from the same total-RNA samples subjected to bulk RNA-seq, as described in the preceding section. Libraries were prepared and sequenced from 5 µg of total RNA as described for mammalian samples (Shi et al. 2020). Synthetic miRNA spike-in RNA oligonucleotides (Supplemental Table S3) were added to each total-RNA sample before size-selection, in proportion to measured RNA content. A detailed protocol for constructing sRNA-seq libraries is available at http://bartellab.wi.mit.edu/protocols.html. Libraries were sequenced on the Illumina NovaSeq platform with 100-nt single-end reads. Processing of the sequencing read data and subsequent analyses was as previously described (Shi et al. 2020). Counting of annotated miRNAs was performed by string-matching the first 19 nt of each read to a dictionary derived from the set of mature miRNA names and sequences downloaded from TargetScanMouse 7 (Agarwal et al. 2015).

Further analyses were performed on miRNA or passenger-strand species passing the expression threshold of at least five matching reads in each of the four libraries derived from a tissue. When calculating normalized abundances, the mean of miRNA counts across two replicates was taken, normalized to the sum of all mean miRNA-matching counts (after removing counts accruing to the synthetic spike-in oligos), and multiplied by 10^6 to yield counts per million (CPM). Differential expression and significance levels were determined using DESeq2 v1.26.0 (Love et al. 2014) without use of the lfcShrink() function, using raw counts as input. For all plotting and analyses, fold-changes observed between *Zswim8*$^{+/-}$ and *Zswim8*$^{-/-}$ samples, as well as their standard errors, were generated by DESeq2.

For identifying miRNAs significantly up-regulated between *Zswim8*$^{+/-}$ and *Zswim8*$^{-/-}$ samples from a tissue, we used a method based on a modified BBUM model (Wang and Bartel 2023). For each tissue, all miRNAs with an FDR-adjusted *P*-value < 0.05 were called as significantly up-regulated. A significantly up-regulated miRNA produced from a single locus was classified as a ZSWIM8-sensitive miRNA if its $\log_2$ fold-change upon *Zswim8* loss was significantly greater than that of its passenger strand, as would be expected of substrates of TDMD under the assumption that the change in the level of the miRNA is affected by ZSWIM8-mediated degradation, but not change in its production rate nor the production or degradation rates of the passenger. Any significantly up-regulated miRNA that did not meet this standard of significance was classified, together with its passenger strand, as secondarily ZSWIM8-sensitive. In the few cases (e.g., two of 33 ZSWIM8-sensitive miRNAs in forebrain) in which the passenger strand was not detected above the count cutoff in a tissue, the significantly up-regulated miRNA was classified as ZSWIM8-sensitive.

Additional miRNAs that were not called as significantly up-regulated were also classified as ZSWIM8-sensitive if they showed increases in at least 11 of 12 *Zswim8*$^{-/-}$ tissues, with a median $\log_2$ fold-change > 0.2 across tissues, as well as a greater increase compared with that of its cognate strand, with a median difference in $\log_2$ fold-change > 0.2 across tissues. Nine miRNAs met these alternative criteria: miR-212-3p, miR-345-3p, miR-351-5p, miR-361-5p, miR-380-3p, miR-466m-3p, miR-744-3p, miR-99b-3p, and miR-497a-3p.

A miRNA that was not called ZSWIM8-sensitive in a tissue was considered marginally sensitive in that tissue if it was classified as ZSWIM8-sensitive in at least one other tissue, MEF, or iNeuron (Shi et al. 2020) and if its $\log_2$ fold-change was significantly greater than that of its passenger strand in the tissue under consideration, as assessed by the method based on standard errors described above.

For analysis of miRNA clusters, mouse miRNA annotations were from TargetScan7 (Agarwal et al. 2015), and their genomic coordinates and associated primary transcript sequences were from miRBase release 22.1 (Kozomara et al. 2019). To focus on confidently annotated miRNAs, a miRNA hairpin locus was only considered for analysis if at least one of its strands was annotated by TargetScan7 as part of a "broadly conserved," "conserved," or "poorly conserved but confidently annotated" miRNA family. A cluster was defined as a set of at least two miRNAs hairpin loci (annotated in miRBase as miRNA primary transcripts) on the same chromosomal strand whose boundaries fell within a contiguously sliding 10-kb window. By this definition, we found the mouse genome to contain 604 annotated miRNA loci, of which 280 collectively resided within 60 clusters. A hairpin locus was counted as encoding a ZSWIM8-sensitive miRNA if either mature strand produced from it was annotated as ZSWIM8-sensitive in an E18.5 tissue, MEF, or iNeuron (Shi et al. 2020).

For arm-switching analysis, the passenger strands produced from all miRNA loci encoding a given ZSWIM8-senstive miRNA were pooled and treated identically, and this pooled passenger strand was compared in abundance to the corresponding ZSWIM8-sensitive strand between the *Zswim8*$^{+/-}$ and *Zswim8*$^{-/-}$ tissues. An arm-switching event was counted in a given tissue if the identity of the more abundant of the two strands associated with a ZSWIM8-sensitive miRNA was observed to depend on the *Zswim8* genotype.

scRNA-seq

scRNA-seq data were generated from dissociated whole lungs dissected from two *Zswim8*$^{+/-}$ and three *Zswim8*$^{-/-}$ E18.5 embryos. For dissociation, each set of lungs was minced on ice with scissors, incubated in 500 µL digestion solution composed of 100 µL collagenase (2000 U/mL, Thermo Fisher Scientific), 16.5 µL DNase I (0.33 U/mL, Roche), and 383.5 µL DMEM/F-12 media (Thermo Fisher Scientific), and rotated end-over-end for 45 min at 37°C. Following dissociation, 500 µL DMEM/F-12 +10% fetal bovine serum (FBS) was added to the reaction, and the suspension was filtered through a 70-µm strainer. The filtrate was pelleted at 400*g* for 5 min at 4°C, resuspended in 500 µL red blood cell lysis buffer (StemCell Technologies) with a wide-bore P1000 tip, incubated for 1 min at room temperature, and again pelleted at 400*g* for 5 min at 4°C. The pellet was resuspended in 200 µL DMEM/F12 +10% FBS with a wide-bore P1000 tip, and cells were counted and assessed for viability by trypan blue staining. For the five samples, viabilities ranged from 64%–81%. Cells were then loaded onto a chromium controller for library preparation using the chromium next GEM single-cell 3′ GEM, library & gel bead kit v3.1 (10x Genomics), targeting 10,000 cells per library, and libraries were sequenced on an Illumina NovaSeq platform with 150-nt paired-end reads.

Sequencing data were aligned to the mouse genome (mm10) and demultiplexing, barcode processing, gene counting, and aggregation were performed using Cell Ranger software v4.0.0 (https://support.10xgenomics.com/single-cell-gene-expression/software/pipelines/latest/what-is-cell-ranger). Processed data were further filtered and analyzed using SCANPY (Wolf et al. 2018). Each library was filtered for cells with detectable counts for more than 200 and fewer than 12,000 genes, each detected in at least three cells, a mitochondrial gene-count percentage of <15%, and a hemoglobin gene-count percentage of <10%. Contributions per cell from total gene counts, percentage of mitochondrial gene counts, and percentage of hemoglobin gene counts were then regressed out. For analyses of all lung cells, the data from all libraries were combined; UMAP was performed with 10 nearest neighbors and 40 principal components; and neighborhood detection was performed using the Leiden clustering method with a resolution parameter of 0.2. Cell counts by genotype and top marker genes for each cluster are listed (Supplemental Table S2). For analyses of alveolar epithelial cells, the cluster characterized by expression of the *Nkx2-1* lineage marker was extracted, as described in the text. On this subset, UMAP was performed with five nearest neighbors and 15 principal components, and clustering was performed with a resolution parameter of 0.4.

miRNA targeting analysis

Predictions of miRNA targets were from TargetScanMouse 7 (Agarwal et al. 2015). Using these annotations, the set of all predicted targets of the miRNA family was taken as the least stringent cohort used for analyses. The set of all conserved predicted targets was taken as the cohort with medium stringency, and the subset of all predicted targets in the top decile of cumulative weighted context++ scores, named the top predicted targets, was taken as the cohort with highest prediction stringency. Finally, the set of all transcripts represented, excluding those predicted as targets of a given family, was used as the pool of transcripts not predicted to be targeted by that family, from which the no-site cohorts were selected.

For analyses of miRNA-mediated repression in a given tissue, the cohorts described above were filtered for transcripts with expression greater than 10 TPM in that tissue for all data sets from both *Zswim8*$^{+/-}$ and *Zswim8*$^{-/-}$ genotypes. For each cohort of predicted targets, a matched no-site cohort was sampled, under the condition that for each predicted target, five no-site transcripts were selected from a bin with matched 3′ UTR length. The

3′ UTR bins were generated by partitioning by length all 3′ UTRs into 20 uniformly populated bins, ranging from the shortest to longest annotated 3′ UTRs in TargetScan.

To compute repression of a predicted-target cohort in a tissue, the distribution of $\log_2$ fold-changes in *Zswim8*$^{-/-}$ relative to *Zswim8*$^{+/-}$ was compared with that of a corresponding no-site cohort using the Mann–Whitney *U* test, and the median $\log_2$ fold-change of the predicted-target cohort was subtracted by that of the no-site cohort to yield a measure of fold repression attributable to a miRNA family. This procedure was repeated 21 times, each with a different randomly sampled no-site cohort, to yield a mean and standard error for fold repression. These values, along with the median *P*-value from the 21 samplings (Mann–Whitney *U* test), are reported for each of the predicted-target cohorts for each of the three most increasing miRNA families in each tissue (Supplemental Fig. S6E).

Histology and immunofluorescence microscopy

For general histological analysis of the heart and lungs, E18.5 embryos were dissected while submerged under ice-cold PBS to prevent breathing of air and preserve developmental anatomy, and the thoracic cavity was exposed for overnight fixation with Bouin's solution, followed by paraffin embedding, serial microtome sectioning with a thickness of 5 µm, and staining with hematoxylin and eosin (H&E). For immunofluorescence experiments, lungs dissected as described above were fixed in 4% paraformaldehyde (Electron Microscopy Sciences) overnight at 4°C, transferred to 30% sucrose for cryoprotection, embedded in Tissue-Tek optimal cutting temperature compound (Sakura Finetek), and sectioned at a thickness of 25 µm using a cryostat microtome (Leica). Tissue sections were stained overnight with the primary antibodies hamster anti-Podoplanin (DSHB 8.1.1; 1:800 dilution), rabbit anti-pro-Surfactant C (Millipore AB3786; 1:1500 dilution) and for 1 h at room temperature with the following fluorescent secondary antibodies: goat anti-hamster IgG AlexaFluor 568 (Invitrogen A-21112; 1:500 dilution), goat anti-rabbit IgG AlexaFluor 647 (Invitrogen A-21245; 1:500 dilution), and NucBlue Hoechst 33342 (Invitrogen; two drops/mL). Fluorescence microscopy was performed on a Nikon Ti widefield microscope.

Data access

All raw and processed sequencing data generated in this study have been submitted to the NCBI Gene Expression Omnibus (GEO; https://www.ncbi.nlm.nih.gov/geo/) under accession number GSE231450.

Competing interest statement

The authors declare no competing interests.

Acknowledgments

We thank M. Frank for assistance with tissue dissections; R. Bronson for assistance with histological analysis; D. Lin, M. Frank, R. Saunders, L. Blodgett, A. Latifkar, E. Kingston, S. McGeary, V. Auyeung, and J. Rajagopal for helpful discussions; A. Ventura, J. Silva, and J. Cavaille for sharing mouse strains; the Whitehead Genetically Engineered Models Center for assistance with generating mouse strains; the Whitehead Genome Technology Core for sequencing; the Koch Institute's Swanson Biotechnology Center's Histology Core for histology; and the W.M. Keck Microscopy Facility for imaging. This work was supported by National Institutes of Health grant GM118135 (to D.P.B.). D.P.B. is an investigator of the Howard Hughes Medical Institute.

Author contributions: C.Y.S. and D.P.B. conceived the project and designed the study. C.Y.S. and J.S. performed mouse husbandry and tissue processing, with assistance from B.K. L.E.E. and C.Y.S. prepared samples for single-cell RNA-sequencing. C.Y.S. prepared all other sequencing libraries and performed sequencing data analysis. C.Y.S. and R.R.C. performed immunofluorescence microscopy. B.K. and R.R.C. advised on pathological analysis. C.Y.S. and D.P.B. drafted the manuscript.

References

Agarwal V, Bell GW, Nam J-W, Bartel DP. 2015. Predicting effective microRNA target sites in mammalian mRNAs. *eLife* **4:** e05005. doi:10.7554/eLife.05005

Ameres SL, Horwich MD, Hung JH, Xu J, Ghildiyal M, Weng Z, Zamore PD. 2010. Target RNA-directed trimming and tailing of small silencing RNAs. *Science* **328:** 1534–1539. doi:10.1126/science.1187058

Anders S, Pyl PT, Huber W. 2015. HTSeq—a Python framework to work with high-throughput sequencing data. *Bioinformatics* **31:** 166–169. doi:10.1093/bioinformatics/btu638

Bartel DP. 2018. Metazoan microRNAs. *Cell* **173:** 20–51. doi:10.1016/j.cell.2018.03.006

Baskerville S, Bartel DP. 2005. Microarray profiling of microRNAs reveals frequent coexpression with neighboring miRNAs and host genes. *RNA* **11:** 241–247. doi:10.1261/rna.7240905

Bitetti A, Mallory AC, Golini E, Carrieri C, Carreño Gutiérrez H, Perlas E, Pérez-Rico YA, Tocchini-Valentini GP, Enright AJ, Norton WHJ, et al. 2018. MicroRNA degradation by a conserved target RNA regulates animal behavior. *Nat Struct Mol Biol* **25:** 244–251. doi:10.1038/s41594-018-0032-x

Cazalla D, Yario T, Steitz JA, Steitz J. 2010. Down-regulation of a host microRNA by a *Herpesvirus saimiri* noncoding RNA. *Science* **328:** 1563–1566. doi:10.1126/science.1187197

Chiang HR, Schoenfeld LW, Ruby JG, Auyeung VC, Spies N, Baek D, Johnston WK, Russ C, Luo S, Babiarz JE, et al. 2010. Mammalian microRNAs: experimental evaluation of novel and previously annotated genes. *Genes Dev* **24:** 992–1009. doi:10.1101/gad.1884710

da Rocha ST, Edwards CA, Ito M, Ogata T, Ferguson-Smith AC. 2008. Genomic imprinting at the mammalian *Dlk1-Dio3* domain. *Trends Genet* **24:** 306–316. doi:10.1016/j.tig.2008.03.011

de la Mata M, Gaidatzis D, Vitanescu M, Stadler MB, Wentzel C, Scheiffele P, Filipowicz W, Großhans H. 2015. Potent degradation of neuronal miRNAs induced by highly complementary targets. *EMBO Rep* **16:** 500–511. doi:10.15252/embr.201540078

Dobin A, Davis CA, Schlesinger F, Drenkow J, Zaleski C, Jha S, Batut P, Chaisson M, Gingeras TR. 2013. STAR: ultrafast universal RNA-seq aligner. *Bioinformatics* **29:** 15–21. doi:10.1093/bioinformatics/bts635

Donnelly BF, Yang B, Grimme AL, Vieux KF, Liu CY, Zhou L, McJunkin K. 2022. The developmentally timed decay of an essential microRNA family is seed-sequence dependent. *Cell Rep* **40:** 111154. doi:10.1016/j.celrep.2022.111154

Eisen TJ, Eichhorn SW, Subtelny AO, Bartel DP. 2020. MicroRNAs cause accelerated decay of short-tailed target mRNAs. *Mol Cell* **77:** 775–785.e8. doi:10.1016/j.molcel.2019.12.004

Fang W, Bartel DP. 2020. MicroRNA clustering assists processing of suboptimal microRNA hairpins through the action of the ERH protein. *Mol Cell* **78:** 289–302.e6. doi:10.1016/j.molcel.2020.01.026

Frank DB, Penkala IJ, Zepp JA, Sivakumar A, Linares-Saldana R, Zacharias WJ, Stolz KG, Pankin J, Lu MQ, Wang Q, et al. 2019. Early lineage specification defines alveolar epithelial ontogeny in the murine lung. *Proc Natl Acad Sci USA* **116:** 4362–4371. doi:10.1073/pnas.1813952116

Friedman RC, Farh KKH, Burge CB, Bartel DP. 2009. Most mammalian mRNAs are conserved targets of microRNAs. *Genome Res* **19:** 92–105. doi:10.1101/gr.082701.108

Ghini F, Rubolino C, Climent M, Simeone I, Marzi MJ, Nicassio F. 2018. Endogenous transcripts control miRNA levels and activity in mammalian cells by target-directed miRNA degradation. *Nat Commun* **9:** 3119. doi:10.1038/s41467-018-05182-9

Han YC, Vidigal JA, Mu P, Yao E, Singh I, González AJ, Concepcion CP, Bonetti C, Ogrodowski P, Carver B, et al. 2015. An allelic series of miR-171/492-mutant mice uncovers functional specialization and cooperation among members of a microRNA polycistron. *Nat Genet* **47:** 766–775. doi:10.1038/ng.3321

Han J, Lavigne CA, Jones BT, Zhang H, Gillett F, Mendell JT. 2020. A ubiquitin ligase mediates target-directed microRNA decay independently

of tailing and trimming. *Science* **370:** eabc9546. doi:10.1126/science.abc9546
Hansen TB, Jensen TI, Clausen BH, Bramsen JB, Finsen B, Damgaard CK, Kjems J. 2013. Natural RNA circles function as efficient microRNA sponges. *Nature* **495:** 384–388. doi:10.1038/nature11993
Herriges M, Morrisey EE. 2014. Lung development: orchestrating the generation and regeneration of a complex organ. *Development* **141:** 502–513. doi:10.1242/dev.098186
Hiramuki Y, Sato T, Furuta Y, Surani MA, Sehara-Fujisawa A. 2015. Mest but not miR-335 affects skeletal muscle growth and regeneration. *PLoS One* **10:** e0130436. doi:10.1371/journal.pone.0130436
Hutter K, Lohmüller M, Jukic A, Eichin F, Avci S, Labi V, Szabo TG, Hoser SM, Hüttenhofer A, Villunger A, et al. 2020. SAFB2 enables the processing of suboptimal stem-loop structures in clustered primary miRNA transcripts. *Mol Cell* **78:** 876–889.e6. doi:10.1016/j.molcel.2020.05.011
Inoue K, Hirose M, Inoue H, Hatanaka Y, Honda A, Hasegawa A, Mochida K, Ogura A. 2017. The rodent-specific microRNA cluster within the *Sfmbt2* gene is imprinted and essential for placental development. *Cell Rep* **19:** 949–956. doi:10.1016/j.celrep.2017.04.018
Jonas S, Izaurralde E. 2015. Towards a molecular understanding of microRNA-mediated gene silencing. *Nat Rev Genet* **16:** 421–433. doi:10.1038/nrg3965
Khvorova A, Reynolds A, Jayasena SD. 2003. Functional siRNAs and miRNAs exhibit strand bias. *Cell* **115:** 209–216. doi:10.1016/S0092-8674(03)00801-8
Kingston ER, Blodgett LW, Bartel DP. 2022. Endogenous transcripts direct microRNA degradation in *Drosophila*, and this targeted degradation is required for proper embryonic development. *Mol Cell* **82:** 3872–3884.e9. doi:10.1016/j.molcel.2022.08.029
Kleaveland B, Shi CY, Stefano J, Bartel DP. 2018. A network of noncoding regulatory RNAs acts in the mammalian brain. *Cell* **174:** 350–362.e17. doi:10.1016/j.cell.2018.05.022
Kozomara A, Birgaoanu M, Griffiths-Jones S. 2019. miRBase: from microRNA sequences to function. *Nucleic Acids Res* **47:** D155–D162. doi:10.1093/nar/gky1141
Labialle S, Marty V, Bortolin-Cavaillé ML, Hoareau-Osman M, Pradère JP, Valet P, Martin PG, Cavaillé J. 2014. The miR-379/miR-410 cluster at the imprinted *Dlk1-Dio3* domain controls neonatal metabolic adaptation. *EMBO J* **33:** 2216–2230. doi:10.15252/embj.201387038
Lee S, Song J, Kim S, Kim J, Hong Y, Kim Y, Kim D, Baek D, Ahn K. 2013. Selective degradation of host microRNAs by an intergenic HCMV noncoding RNA accelerates virus production. *Cell Host Microbe* **13:** 678–690. doi:10.1016/j.chom.2013.05.007
Li X, Pritykin Y, Concepcion CP, Lu Y, La Rocca G, Zhang M, King B, Cook PJ, Au YW, Popow O, et al. 2020. High-resolution *in vivo* identification of miRNA targets by halo-enhanced Ago2 pulldown. *Mol Cell* **79:** 167–179.e11. doi:10.1016/j.molcel.2020.05.009
Li L, Sheng P, Li T, Fields CJ, Hiers NM, Wang Y, Li J, Guardia CM, Licht JD, Xie M. 2021. Widespread microRNA degradation elements in target mRNAs can assist the encoded proteins. *Genes Dev* **35:** 1595–1609. doi:10.1101/gad.348874.121
Libri V, Helwak A, Miesen P, Santhakumar D, Borger JG, Kudla G, Grey F, Tollervey D, Buck AH. 2012. Murine cytomegalovirus encodes a miR-27 inhibitor disguised as a target. *Proc Natl Acad Sci USA* **109:** 279–284. doi:10.1073/pnas.1114204109
Llobet-Navas D, Rodríguez-Barrueco R, Castro V, Ugalde AP, Sumazin P, Jacob-Sendler D, Demircan B, Castillo-Martín M, Putcha P, Marshall N, et al. 2014. The *miR-424(322)/503* cluster orchestrates remodeling of the epithelium in the involuting mammary gland. *Genes Dev* **28:** 765–782. doi:10.1101/gad.237404.114
Love MI, Huber W, Anders S. 2014. Moderated estimation of fold change and dispersion for RNA-seq data with DESeq2. *Genome Biol* **15:** 550. doi:10.1186/s13059-014-0550-8
Lu Y, Thomson JM, Wong HYF, Hammond SM, Hogan BLM. 2007. Transgenic over-expression of the microRNA *miR-17-92* cluster promotes proliferation and inhibits differentiation of lung epithelial progenitor cells. *Dev Biol* **310:** 442–453. doi:10.1016/j.ydbio.2007.08.007
Marcinowski L, Tanguy M, Krmpotic A, Rädle B, Lisnić VJ, Tuddenham L, Chane-Woon-Ming B, Ruzsics Z, Erhard F, Benkartek C, et al. 2012. Degradation of cellular miR-27 by a novel, highly abundant viral transcript is important for efficient virus replication *in vivo*. *PLoS Pathog* **8:** e1002510. doi:10.1371/journal.ppat.1002510
Marty V, Labialle S, Bortolin-Cavaillé ML, De Medeiros GF, Moisan MP, Florian C, Cavaillé J. 2016. Deletion of the miR-379/miR-410 gene cluster at the imprinted *Dlk1-Dio3* locus enhances anxiety-related behaviour. *Hum Mol Genet* **25:** 728–739. doi:10.1093/hmg/ddv510
Mavroudis C, Backer CL, Jacobs JP, Anderson RH. 2013. Ventricular septal defect. In *Pediatric cardiac surgery* (ed. Mavroudis C, et al.), pp. 311–341. John Wiley and Sons, Ltd., Hoboken, NJ. doi:10.1002/9781118320754.ch17
McInnes L, Healy J, Saul N, Großberger L. 2018. UMAP: Uniform Manifold Approximation and Projection. *J Open Source Softw* **3:** 861. doi:10.21105/joss.00861
Memczak S, Jens M, Elefsinioti A, Torti F, Krueger J, Rybak A, Maier L, Mackowiak SD, Gregersen LH, Munschauer M, et al. 2013. Circular RNAs are a large class of animal RNAs with regulatory potency. *Nature* **495:** 333–338. doi:10.1038/nature11928
Molina-Pelayo C, Olguin P, Mlodzik M, Glavic A. 2022. The conserved Pelado/ZSWIM8 protein regulates actin dynamics by promoting linear actin filament polymerization. *Life Sci Alliance* **5:** e202201484. doi:10.26508/lsa.202201484
Morrisey EE, Hogan BLM. 2010. Preparing for the first breath: genetic and cellular mechanisms in lung development. *Dev Cell* **18:** 8–23. doi:10.1016/j.devcel.2009.12.010
Okumura F, Oki N, Fujiki Y, Ikuta R, Osaki K, Hamada S, Nakatsukasa K, Hisamoto N, Hara T, Kamura T. 2021. ZSWIM8 is a myogenic protein that partly prevents C2C12 differentiation. *Sci Rep* **11:** 20880. doi:10.1038/s41598-021-00306-6
Schwarz DS, Hutvágner G, Du T, Xu Z, Aronin N, Zamore PD. 2003. Asymmetry in the assembly of the RNAi enzyme complex. *Cell* **115:** 199–208. doi:10.1016/S0092-8674(03)00759-1
Seitz H, Youngson N, Lin SP, Dalbert S, Paulsen M, Bachellerie JP, Ferguson-Smith AC, Cavaillé J. 2003. Imprinted microRNA genes transcribed antisense to a reciprocally imprinted retrotransposon-like gene. *Nat Genet* **34:** 261–262. doi:10.1038/ng1171
Shang R, Baek SC, Kim K, Kim B, Kim VN, Lai EC. 2020. Genomic clustering facilitates nuclear processing of suboptimal pri-miRNA loci. *Mol Cell* **78:** 303–316.e4. doi:10.1016/j.molcel.2020.02.009
Sheng P, Li L, Li T, Wang Y, Hiers NM, Mejia JS, Sanchez JS, Zhou L, Xie M. 2023. Screening of *Drosophila* microRNA-degradation sequences reveals Argonaute1 mRNA's role in regulating miR-999. *Nat Commun* **14:** 2108. doi:10.1038/s41467-023-37819-9
Sheu-Gruttadauria J, Pawlica P, Klum SM, Wang S, Yario TA, Schirle Oakdale NT, Steitz JA, MacRae IJ. 2019. Structural basis for target-directed microRNA degradation. *Mol Cell* **75:** 1243–1255.e7. doi:10.1016/j.molcel.2019.06.019
Shi CY, Kingston ER, Kleaveland B, Lin DH, Stubna MW, Bartel DP. 2020. The ZSWIM8 ubiquitin ligase mediates target-directed microRNA degradation. *Science* **370:** eabc9359. doi:10.1126/science.abc9359
Truett GE, Heeger P, Mynatt RL, Truett AA, Walker JA, Warman ML. 2000. Preparation of PCR-quality mouse genomic DNA with hot sodium hydroxide and tris (HotSHOT). *Biotechniques* **29:** 52–54. doi:10.2144/00291bm09
Ventura A, Young AG, Winslow MM, Lintault L, Meissner A, Erkeland SJ, Newman J, Bronson RT, Crowley D, Stone JR, et al. 2008. Targeted deletion reveals essential and overlapping functions of the *miR-17~92* family of miRNA clusters. *Cell* **132:** 875–886. doi:10.1016/j.cell.2008.02.019
Wang PY, Bartel DP. 2023. A statistical approach for identifying primary substrates of ZSWIM8-mediated microRNA degradation in small-RNA sequencing data. *BMC Bioinformatics* **24:** 195. doi:10.1186/s12859-023-05306-z
Wang Z, Hou Y, Guo X, van der Voet M, Boxem M, Dixon JE, Chisholm AD, Jin Y. 2013. The EBAX-type Cullin-RING E3 ligase and Hsp90 guard the protein quality of the SAX-3/Robo receptor in developing neurons. *Neuron* **79:** 903–916. doi:10.1016/j.neuron.2013.06.035
Wang Y, Frank DB, Morley MP, Zhou S, Wang X, Lu MM, Lazar MA, Morrisey EE. 2016. HDAC3-dependent epigenetic pathway controls lung alveolar epithelial cell remodeling and spreading via miR-17-92 and TGF-β signaling regulation. *Dev Cell* **36:** 303–315. doi:10.1016/j.devcel.2015.12.031
Wang G, Lei J, Wang Y, Yu J, He Y, Zhao W, Hu Z, Xu Z, Jin Y, Gu Y, et al. 2023. The ZSWIM8 ubiquitin ligase regulates neurodevelopment by guarding the protein quality of intrinsically disordered Dab1. *Cereb Cortex* **33:** 3866–3881. doi:10.1093/cercor/bhac313
Whipple AJ, Breton-Provencher V, Jacobs HN, Chitta UK, Sur M, Sharp PA. 2020. Imprinted maternally expressed microRNAs antagonize paternally driven gene programs in neurons. *Mol Cell* **78:** 85–95.e8. doi:10.1016/j.molcel.2020.01.020
Wolf FA, Angerer P, Theis FJ. 2018. SCANPY: large-scale single-cell gene expression data analysis. *Genome Biol* **19:** 15. doi:10.1186/s13059-017-1382-0
Xie J, Ameres SL, Friedline R, Hung J-H, Zhang Y, Xie Q, Zhong L, Su Q, He R, Li M, et al. 2012. Long-term, efficient inhibition of microRNA function in mice using rAAV vectors. *Nat Methods* **9:** 403–409. doi:10.1038/nmeth.1903

Received May 4, 2023; accepted in revised form July 31, 2023.

ZSWIM8 destabilizes many murine microRNAs and is required for proper embryonic growth and development

Charlie Y. Shi, Lara E. Elcavage, Raghu R. Chivukula, et al.

Genome Res. 2023 33: 1482-1496 originally published online August 2, 2023
Access the most recent version at doi:10.1101/gr.278073.123